Early Earth's Phaneritic Ultramafic Rocks: Plate Tectonic Mantle Slices or Crustal Cumulates?

Jiawei Zuo[1]*, A. Alexander G. Webb[1]*, Emily J. Chin[2], Jason Harvey[3], Peter J. Haproff[4], Thomas Müller[3,5], Qin Wang[6], Lukáš Ackerman[7], Arthur H. Hickman[8], Dominik Sorger[5], Anthony Ramírez-Salazar[3],

[1]Division of Earth and Planetary Science and Laboratory for Space Research, University of Hong Kong, Pokfulam Road, Hong Kong, China

[2]Scripps Institution of Oceanography, University of California, San Diego, La Jolla, California 92093, USA

[3]School of Earth and Environment, University of Leeds, Leeds LS2 9JT, UK

[4]Department of Earth and Ocean Sciences, University of North Carolina Wilmington, North Carolina 28403, USA

[5]Geoscience Center, Department of Mineralogy, Georg-August-Universität Göttingen, D-37077 Göttingen, Germany

[6]State Key Laboratory for Mineral Deposits Research, School of Earth Sciences and Engineering, Nanjing University, Nanjing 210046, China

[7]Institute of Geology of the Czech Academy of Sciences, Rozvojová 269, Prague 6, 16500, Czech Republic

[8]Geological Survey of Western Australia, 100 Plain St., East Perth, Western Australia 6004, Australia.

*Corresponding authors: Jiawei Zuo (jwzuo@connect.hku.hk), Alexander Webb (aagwebb@hku.hk)

Key points:

1. Ultramafic rocks of the Isua supracrustal belt and the East Pilbara Terrane can be interpreted as crustal cumulates.
2. A crustal cumulate interpretation is not diagnostic – these rocks can form in all proposed Archean tectonic settings.
3. Ultramafic rocks of the Isua supracrustal belt do not require >3.7 Ga plate tectonics.

Abstract:

How and when plate tectonics initiated remain uncertain. In part, this is because many signals that have been interpreted as diagnostic of plate tectonics can be alternatively explained via hot stagnant-lid tectonics. One such signal involves early Archean phaneritic ultramafic rocks. In the Eoarchean Isua supracrustal belt of southwestern Greenland, some ultramafic rocks have been interpreted as mantle rocks tectonically exhumed during Eoarchean subduction. To explore whether all Archean phaneritic ultramafic rocks originated as cumulate and/or komatiite – i.e., without requiring plate tectonics – we examined the petrology and geochemistry of such rocks in the Isua supracrustal belt and the Paleoarchean East Pilbara Terrane of northwestern Australia, with Pilbara ultramafic rocks being representative of rocks from non-plate tectonic settings. We found that Pilbara ultramafic samples have cumulate textures and relative enrichment of whole-rock Os, Ir, and Ru versus Pt. In comparison, polygonal textures and variable whole-rock Os, Ir, Ru and Pt patterns are identified in Isua ultramafic samples. Isua and Pilbara ultramafic samples have (1) mineral assemblages that can form at crustal conditions; (2) broadly similar whole-rock major element patterns; (3) weakly fractionated to unfractionated trace element patterns that are close to primitive mantle values; and (4) spinel with variable TiO_2, relatively consistent Cr#, and variable and low Mg#. Many features of Isua or Pilbara ultramafic rocks are similar to depleted mantle rocks, except for spinel chemistry and cumulate textures. However, all features are consistent with cumulates. Collectively, these data permit ≤ 3.2 Ga initiation of plate tectonics on Earth.

Plain Language Summary:

Earth's rigid outer shell is broken into pieces that move relative to each other. These motions are generally understood according to the theory of plate tectonics. However, the origins of plate tectonics are not well understood. This contribution focuses on an aspect of this problem, namely, the lack of consensus concerning when plate tectonics started. We examine some of the most ancient evidence which has been speculated to record plate tectonic processes: ultramafic rocks from the ≥3.7 billion-years-old Isua supracrustal belt of southwestern Greenland. A leading hypothesis suggests that these are mantle (deep) rocks emplaced by plate tectonic deformation. We test the viability of an alternative hypothesis: that these rocks may have crystallized from magmas at crustal (shallow) levels, a history that would not require plate tectonics. Specifically, we compare new and published mineral and chemical features of the Isua ultramafic rocks with similar rocks from known crustal and mantle settings, including new data from a northwestern Australia crustal site which is similar, yet non-plate tectonic. Results show that each feature of the Isua ultramafic rocks is consistent with crustal crystallization. Therefore, these rocks do not constrain early plate tectonics, which could have developed later.

1. Introduction:

When, how, and why plate tectonics began on Earth remain among the most important unresolved questions in plate tectonic theory (e.g., Bauer et al., 2020; Beall et al., 2018; Brown and Johnson, 2018; Condie and Puetz, 2019; Hansen, 2007; Harrison, 2009; Korenaga, 2011; Nutman et al., 2020; Stern, 2008; Tang et al., 2020). Investigations of plate tectonic initiation have significant implications for questions associated with the evolution of early terrestrial planets, including (1) whether early Earth experienced any pre-plate tectonic global geodynamics/cooling after the magma ocean stage (e.g., Bédard, 2018; Collins et al., 1998; Lenardic, 2018; Moore and Webb, 2013; O'Neill and Debaille, 2014); and (2) why other terrestrial planets in the solar system appear to lack plate tectonic records (e.g., Moore et al., 2017; Stern et al., 2017; cf. Yin, 2012a; Yin, 2012b).

Many proposed signals for the initiation or early operation of plate tectonics on Earth are controversial due to the issue of non-uniqueness. For instance, the origin of Hadean zircons from the Jack Hills of western Australia have been contrastingly interpreted as (1) detrital crystals from felsic magmas generated by ~4.3 Ga plate subduction (Harrison, 2009; Hopkins et al., 2008); (2) zircons crystallized via impact heating and ejecta sheet burial (Marchi et al., 2014) or (3) low pressure melting of Hadean mafic crustal materials (Reimink et al., 2020). Similarly, researchers continue to debate whether the presence of Archean low-Ti mafic lava (also termed as boninite or boninitic basalts) must indicate subduction initiation as early as ~3.7 Ga (cf. Pearce and Reagan, 2019; Polat and Hofmann, 2003). Another example is how a ~3.2 Ga shift in zircon Hf-isotope signatures has been variably interpreted to indicate the onset of plate tectonics (Næraa et al., 2012) or enhanced mantle melting during a proposed Earth's thermal peak (Kirkland et al., 2021). Due to these equivocal interpretations, the initiation of plate tectonics has been suggested to be ≤3.2 Ga using geological records that are generally considered unique to plate tectonics (e.g., paired metamorphic belts, ultra-high pressure terranes, and passive margins) (e.g., Brown and Johnson, 2018; Cawood et al., 2018; Stern, 2008; cf. Bauer et al., 2020; Foley et al., 2014; Harrison, 2009; Korenaga, 2011; Nutman et al., 2020). The ≤3.2 Ga onset of plate tectonics requires early Earth tectonic evolution to be non-uniformitarian, involving some form of single-plate stagnant-lid tectonics (e.g., Bédard, 2018; Collins et al., 1998; Moore and Webb, 2013).

One proposed signal of early plate tectonics is the preservation of phaneritic ultramafic rocks in Eo- and Paleoarchean terranes. However, the issue of non-uniqueness also extends to their interpretations. In the Eoarchean Isua supracrustal belt and adjacent meta-tonalite bodies exposed in southwestern Greenland (**Fig. 1a**), some dunites and harzburgites have been interpreted to represent melt-depleted mantle rocks that were emplaced on top of crustal rocks during the Eoarchean plate tectonic subduction (e.g., Friend and Nutman, 2011; Nutman et al., 2020; Van de Löcht et al., 2018), similar to how modern ophiolitic ultramafic rocks are preserved in collisional massifs (e.g., Boudier et al., 1988; Lundeen, 1978; Wal and Vissers, 1993). In contrast, Szilas et al. (2015) argue that dunites and harzburgites in the Isua supracrustal belt can be interpreted as crustal cumulates based on their geochemical signatures. Crustal cumulates are not exclusive to plate tectonics, and have been used to explain the emplacement of other phaneritic ultramafic rocks in Eo- and Paleoarchean terranes. Examples include phaneritic ultramafic rocks in the Eoarchean Tussapp ultramafic complex of southwestern Greenland (McIntyre et al., 2019), the Paleoarchean East Pilbara Terrane of northwestern Australia (e.g., Smithies et al., 2007), and the Paleoarchean Barberton Greenstone Belt of South Africa (e.g., Byerly et al., 2019). Therefore, ultramafic rocks in the Isua supracrustal belt potentially formed in a different tectonic setting compared to those of other early Archean terranes. Because all early Archean terranes preserve voluminous tonalite-trondhjemite-granodiorite (TTG) suites surrounded by deformed, dominantly mafic supracrustal belts (e.g., **Fig. 1**; also Condie, 2019), a different origin for the Isua supracrustal belt may be an artifact of interpretive non-uniqueness. If the phaneritic ultramafic rocks of the Isua supracrustal belt can be similarly interpreted to have cumulate or volcanic origins (which is questioned by many recent studies, see section 2 for a review), then these rocks cannot be used as unequivocal indicators of plate tectonics.

This contribution explores the origins of Isua ultramafic rocks via analysis of new and published geochemical and petrological findings, including comparative analysis of the key Isua rocks and similar rocks from settings considered representative of hot stagnant-lid tectonics [In this study, we follow tectonic taxonomy from Lenardic (2018)]. The Paleoarchean geology of the East Pilbara Terrane is widely accepted as representing hot stagnant-lid tectonics (Hickman, 2021; Johnson et al., 2014; Smithies et al., 2007, 2021; Van Kranendonk et al., 2004, 2007); Pilbara ultramafic samples are also investigated in this study (**Fig. 1b**) as examples of ultramafic rocks from non-plate tectonic regimes. We also compare the petrology and geochemistry of Isua ultramafic rocks with compiled (1) ultramafic cumulate rocks; (2) modelled ultramafic cumulate rocks; (3) melt-depleted mantle rocks from plate tectonic settings; and (4) modelled melt-depleted mantle rocks. We then examine whether the generation of Isua and Pilbara ultramafic rocks is compatible with the predictions of hot stagnant-lid tectonics. Our findings help to evaluate whether plate tectonics is indeed required to explain the Eoarchean assembly of the Isua supracrustal belt.

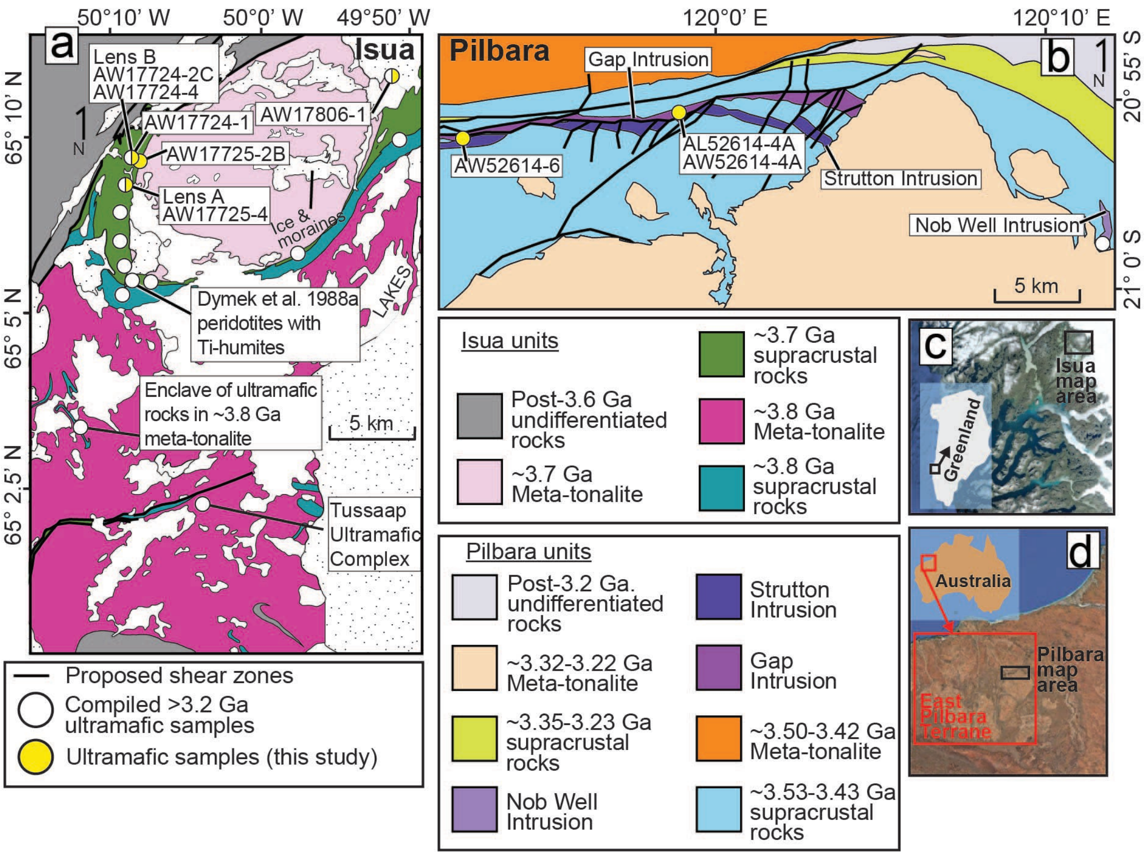

Figure 1. Geological maps of the Isua supracrustal belt, southwestern Greenland and north-central portion of the East Pilbara Terrane, northwestern Australia. **a**: simplified geology of the Isua supracrustal belt and adjacent areas [modified from Nutman et al. (2002)]. Locations of meta-peridotite enclaves and lenses A and B are presented. **b**: simplified geology of the north edge of the Mount Edgar Complex [modified from Van Kranendonk et al. (2007)] showing major km-scale ultramafic intrusive bodies: the Gap Intrusion, the Nob Webb Intrusion, and the Strutton Intrusion. **c:** location of the Isua supracrustal belt in southwestern Greenland. **d:** location of the East Pilbara Terrane in northwestern Australia. Yellow circles: locations for new samples; white circles, locations for compiled samples from Szilas et al. (2015), Van de Löcht et al. (2018), Friend et al. (2002), Friend and Nutman (2011), McIntyre et al. (2019), Dymek et al. (1988). and the Geological Survey of Western Australia 2013 database.

2. Geological background and proposed tectonic models

2.1.The Isua supracrustal belt

The ~35 km-long, ~1 to 4 km-wide Isua supracrustal belt of southwestern Greenland is Earth's largest recognized Eoarchean terrane (**Fig. 1a**). The belt's protoliths were formed during ~3.8 Ga to ~3.7 Ga and experienced extensive shearing, thinning, and folding (e.g., Nutman et al., 2020; Webb et al., 2020). Regional deformation of the Isua supracrustal belt is associated with amphibolite facies assemblages that have been interpreted to be Eoarchean (e.g., Nutman et al., 2020; Webb et al., 2020; Ramirez-Salazar et al., 2021; Zuo et al., 2021) and/or Neoarchean in age (e.g., Chadwick, 1990; Nutman, 1986; Nutman et al., 2015). Meta-tonalites of similar ages to the ~3.8 to 3.7 Ga supracrustal rocks are in contact with the Eoarchean supracrustal belt to the north and south (Crowley et al., 2002; Crowley, 2003). The interior of the belt exposes metamorphosed basalts chert, banded iron formation, and voluminously minor metamorphosed ultramafic igneous rocks, felsic volcanic rocks, and detrital sedimentary rocks (e.g., Komiya et al., 1999; Nutman et al., 2002; Nutman and Friend, 2009)

Ultramafic rocks in the Isua supracrustal belt occur as ~1- to ~100-m-scale lenticular bodies associated with mafic pillow lavas (e.g., Dymek et al., 1988b; Szilas et al., 2015) or as enclaves in both north and south meta-tonalite bodies (e.g., Friend et al., 2002; Nutman and Friend, 2009). These ultramafic rocks appear to have experienced various degrees of alteration including carbonitization and serpentinization (e.g., Dymek et al., 1988b; Friend et al., 2002; Szilas et al., 2015). Two ~10^4 m^2 meta-peridotite lenses (a southern lens A and a northern lens B) located ~1.5-km apart along the eastern edge of the western Isua supracrustal belt and some ultramafic enclaves (as large as ~10^4 m^2) in meta-tonalite located ~15 km south of the belt (**Fig. 1a**) contain dunites and/or harzburgites with relatively weak carbonitization and serpentinization. Igneous, metamorphic and deformation features of these dunites and harzburgites have been explored to constrain the Eoarchean tectonic evolution of the Isua supracrustal belt (e.g., Kaczmarek et al., 2016; Nutman et al., 2020; Van de Löcht et al., 2018). These features include: (1) primary rock textures and deformation overprints, such as polygonal textures and B-type olivine deformation fabrics observed in dunites from the meta-peridotite lenses A and B in the Isua supracrustal belt (Kaczmarek et al., 2016; Nutman et al., 1996); (2) a mineral assemblage of olivine + serpentine ± pyroxene ± Ti-humite ± carbonate ± spinel ± ilmenite ± magnesite for dunites from lenses A and B (e.g., Guotana et al., 2021; Nutman et al., 2020; Szilas et al., 2015 and a mineral assemblage of olivine + serpentine + pyroxene + spinel ± hornblende for meta-peridotites from the ultramafic enclaves (Van de Löcht et al., 2018, 2020); (3) primitive mantle-normalized rare earth element patterns (REE) that are sub-parallel to those of nearby basalts (e.g., Szilas et al., 2015; Van de Löcht et al., 2020) or komatiite (Dymek et al., 1988b); and (4) various highly siderophile element (HSE) patterns, including relatively a high primitive mantle-normalized (PM-normalized) Os, Ir and Ru versus to Pt and Pd pattern preserved in ultramafic enclaves in the south meta-tonalite (Van de Löcht et al., 2018), and similar or opposite patterns preserved in the two meta-peridotite lenses of the Isua supracrustal belt (Szilas et al., 2015).

The Isua supracrustal belt has been mostly interpreted to record ~3.8 to 3.6 Ga plate tectonic processes including subduction and subsequent extension (e.g., Arai et al., 2015; Komiya et al., 1999; Nutman et al., 2020; Nutman et al., 2013b; Nutman and Friend, 2009). There are two main competing plate tectonic models for the development of the belt that predict opposite subduction vergences during the Eoarchean. One model that involves southward subduction describes the belt as an Eoarchean accretionary prism, and has no specific prediction for the generation and emplacement of the ultramafic rocks (e.g., Arai et al., 2015; Komiya et al., 1999). In an alternative model, the Isua supracrustal belt initially formed via intra-oceanic arc magmatism during northward subduction and the subsequent collision of multiple arc terranes at ~3.7 Ga (e.g., Nutman et al., 2020). In this model, both the tonalites and supracrustal materials were mostly generated by partial melting of materials from the mantle wedge, subducting slab, or lowermost crust (e.g., Nutman et al., 2013a; Nutman et al., 2020). The only exception is the presence of the dunite- and harzburgite-hosting ultramafic enclaves and two lenses described above, which have been proposed to represent relict melt-depleted mantle rocks thrust atop crustal rocks in a subduction setting (see Figure 8 of Nutman et al., 2013a). As such, (1) the geochemical associations with local basalts are interpreted to reflect melt-rock reactions between basaltic melts and depleted mantle residues (Friend and Nutman, 2011; Van de Löcht et al., 2020); (2) a specific HSE pattern (i.e., relative depletion of Pt, Pd, and Re versus Os, Ir, and Ru) found in ultramafic enclaves enveloped by meta-tonalites located south of the Isua supracrustal belt (**Fig. 1a**) is thought to reflect fractionation during melt depletion in the mantle (Van de Löcht et al., 2018); (3) polygonal rock textures are interpreted to record equilibration under mantle conditions (e.g., Nutman et al., 1996), whereas the B-type olivine fabrics are claimed to exclusively indicate deformation in hydrous mantle wedge environments (Kaczmarek et al., 2016, and references therein); (4) the occurrence of an olivine + antigorite ± Ti-humite mineral assemblage in some dunitic Isua ultramafic rocks is interpreted as evidence of low-temperature, ultrahigh-pressure (UHP) metamorphism (<500 °C , >2.6 GPa) that may be only compatible with a subduction setting (Nutman et al., 2020); (5) the oxygen isotope signatures of some dunitic Isua ultramafic rocks from lens A or lens B are considered to be indicative of metasomatism by mantle-derived fluids, or of metamorphic growth of olivine during the interpreted UHP metamorphism, respectively (Nutman et al., 2021); and (6) clinopyroxene inclusions in olivine of Isua ultramafic rocks from lens A are interpreted to represent re-equilibration between ascending melts and melt-depleted mantle peridotites (Nutman et al., 2021).

Recently, a heat-pipe model (i.e., a subcategory of hot stagnant-lid tectonics) was proposed as an alternative to plate tectonics for the formation and deformation of the Isua supracrustal belt (Webb et al., 2020). Like other hot stagnant-lid tectonic models (e.g., Collins et al., 1998; Johnson et al., 2014), heat-pipe tectonics is dominated by (sub-)vertical transportation of materials, but the main driving force of this transportation is volcanic advection rather than gravitational instability (Moore and Webb, 2013; O'Reilly and Davies, 1981). Voluminous mafic volcanism causes extensive volcanic resurfacing as well as burial and downwards advection of cold surface materials. At great depths, portions of buried hydrated mafic crust are partially melted, forming tonalitic melts. Crustal deformation of a heat-pipe lithosphere is predicted to happen via (1) radial shortening due to subsidence of crustal materials in Earth's quasi-spherical geometry (Bland and McKinnon, 2016; Webb et al., 2020); or (2) contraction during a plate-breaking and subduction event as or soon after the heat-pipe cooling ceases (Beall et al., 2018; Webb et al., 2020). Alternatively, deformation of a fragment of a heat-pipe lithosphere may be possible at any time when involved in a younger deformation zone of any tectonic setting. As to the formation of ultramafic rocks, this model does not involve the thrusting of mantle rocks atop crustal rocks, as subduction and associated mantle wedge settings do not occur during heat-pipe cooling. In this model, the Eoarchean Isua supracrustal belt and adjacent meta-tonalites were initially formed from ~3.8 to ~3.7 Ga via heat-pipe volcanism and lower crust partial melting, and all ultramafic rocks would be crustal cumulates or ultramafic lavas. The features of Isua ultramafic rocks which had previously been interpreted in a plate tectonic context, as enumerated in the prior paragraph, can be alternatively interpreted as follows: (1) the geochemical relationships between Isua ultramafic rocks and nearby basalts reflect contamination of ultramafic lava or cumulate mush by co-existing fluids/melts; (2) the observed fractionated HSE patterns were produced by partitioning during fractional crystallization; (3) the rock textures of Isua ultramafic rocks were produced by crystallization of melts and/or subsequent deformation/mineral re-equilibration under crustal conditions; and (4) the mineral assemblages of these ultramafic rocks, (5) fluid metasomatism, and (6) clinopyroxene inclusions in olivine all formed under crustal conditions.

2.2.The East Pilbara Terrane

The ~40,000 km^2 East Pilbara Terrane of northwestern Australia is the largest and best-preserved Paleoarchean terrane on Earth (**Fig. 1b**). There, eleven granitoid bodies (mostly meta-tonalites, with minor granites) are surrounded by broadly coeval supracrustal belts. These supracrustal belts are dominantly comprised of metamorphosed mafic to felsic volcanic rocks, with some chemical and clastic sedimentary rocks, and ultramafic layered rocks and intrusions (e.g., Van Kranendonk et al., 2007; Hickman, 2021). Rock formation, deformation, and metamorphism (largely greenschist facies) in the East Pilbara Terrane are thought to mostly occur from ~3.5 to 3.2 Ga, such that by the end of the Paleoarchean, the supracrustal belts had been deformed into synforms and the granitoids had become domes (Collins et al., 1998; Van Kranendonk et al., 2007). This regional “dome-and-keel” geometry is a key element for tectonic interpretations of the East Pilbara Terrane.

Ultramafic rocks of the East Pilbara Terrane occur as layers or pods interleaved with supracrustal rocks or as km-scale igneous bodies intruding supracrustal sequences (e.g., Smithies et al., 2007). Ultramafic layers and pods found in the supracrustal sequences commonly have thicknesses of ~1 to 5 meters and, preserve spinifex textures in some locations. These rocks have been interpreted to have been crystallized from komatiitic or basaltic lava flows (e.g., Smithies et al., 2007; Van Kranendonk et al., 2007). In this study, we focus on the km-scale intrusions. In the East Pilbara Terrane, ultramafic rocks are exposed as three >10-km-long and >100-m-thick ultramafic intrusive bodies (**Fig. 1b**), which include the Gap Intrusion, the Strutton Intrusion, and the Nob Well Intrusion. These ultramafic bodies intrude ~3.53 to 3.43 Ga supracrustal sequences and are intruded themselves by ~3.31 Ga granodiorites (**Fig. 1b**) (Williams, 1999). Existing knowledge of these ultramafic rocks is mostly limited to map relationships, petrological descriptions and geochemical data published by the Geological Survey of Western Australia (e.g., Williams, 1999). In general, these ultramafic intrusions are comprised of variably metamorphosed peridotite (including dunite), pyroxenite, and gabbro (Geological Survey of Western Australia 2013 database).

It is now broadly accepted that the East Pilbara Terrane represents a Paleoarchean terrane formed via regional hot stagnant-lid tectonics that featured vigorous (ultra)mafic and felsic volcanism (e.g., Collins et al., 1998; Johnson et al., 2017; François et al., 2014; Moore and Webb, 2013; Van Kranendonk et al., 2007; Van Kranendonk, 2010; Wiemer et al., 2018). One subcategory of this tectonic regime is the partial convective overturn cooling model, which was initially proposed based on the geology of the East Pilbara Terrane (Collins et al., 1998). This model predicts that the East Pilbara Terrane experienced episodic supracrustal volcanism and tonalite formation followed by quiescence during ~10 to ~100 million years cycles of mantle plume activities. (Ultra)mafic magmatism associated with mantle plumes can produce km-scale ultramafic intrusions with or without fractional crystallization (e.g., Smithies, 2007). The partial convective overturn cooling model involves gravitational instability between the relatively hot, buoyant tonalite bodies and colder, denser supracrustal materials. Such instability could lead to diapiric rise of tonalites, with supracrustal rocks deformed into synclines that wrap around the tonalite domes, creating the observed "dome-and-keel" geometry. No subduction activity and associated mantle-derived ultramafic rocks are predicted at the crustal levels of a partial convective overturn lithosphere (e.g., Collins et al., 1998).

3. Methods:

Three ultramafic samples (AL52614-4A, AW52614-4A, and AW52614-6) collected from the Gap Intrusion of the East Pilbara Terrane and six samples (AW17724-1, AW17724-2C, AW17724-4, AW17725-2B, AW17725-4 and AW17806-1) collected from the Isua supracrustal belt were analyzed in this study (**Fig. 1**). Isua samples AW17724-2C, AW17724-4 (northern lens B) and AW17725-4 (southern lens A) were collected from the two meta-peridotite lenses which have been interpreted previously as tectonic mantle slices (e.g., Friend and Nutman, 2011; Nutman et al., 2020)]. Isua sample AW17724-1 was collected from the serpentinite layer enveloping the meta-peridotite lens B. Isua sample AW17725-2B was collected from an ultramafic outcrop near the northern meta-tonalite, ~300 meters east of the lens B. Isua sample AW17806-1 was collected from an outcrop located at the eastern supracrustal belt near the northern meta-tonalite body (**Fig. 1a, Table 1**). To test models of their petrogenesis, we compiled literature data and inspected our samples using thin section petrography and acquisition of (1) whole-rock major/trace element data (Table S1); (2) spinel geochemistry (Table S2); and (3) HSE abundances (Table S3). Compiled Isua and Pilbara data include results of previous studies focused on ultramafic rocks located adjacent to our sample locations. These outcrops specifically include (1) ultramafic rocks collected across the Isua supracrustal belt (including the meta-peridotite lenses) studied by Szilas et al. (2015) and Friend and Nutman (2011) (**Fig. 1a**); (2) ultramafic rocks from the enclaves within the meta-tonalite located south of the Isua supracrustal belt (Van de Löcht et al., 2018); and (3) ultramafic rocks from the Nob Well Intrusion of the East Pilbara Terrane (Geological Survey of Australia 2013 database; **Fig. 1b**). Data from other ultramafic rocks that have been variably interpreted as cumulates or mantle peridotites (see Figures 3–8 captions for references) are compiled for comparison with the ultramafic lithologies of this study. These rocks were collected from variably deformed and altered Archean ultramafic complexes (e.g., McIntyre et al., 2019), massive layered intrusions (e.g., Coggon et al., 2015), collisional massifs (e.g., Wang et al., 2013), volcanic xenoliths (e.g., Ionov, 2010) or mantle rocks extracted from ocean drilling (e.g., Parkinson and Pearce, 2008).

3.1. Analytical details

The whole-rock major element concentrations of Pilbara ultramafic samples were analyzed in the Peter Hooper GeoAnalytical Laboratory at Washington State University. Major elements (e.g. MgO, FeOt, and SiO_2) were analyzed using a Thermo-ARL Advant'XP+ sequential X-ray fluorescence spectrometer (XRF). Sample preparation, analytical conditions, and precisions/accuracy of the analyses follow procedures detailed in Johnson et al. (1999). The whole-rock major element concentrations of Isua ultramafic samples were determined at the State Key Laboratory for Mineral Deposit Research in Nanjing University, China. Small fresh rock pieces of Isua ultramafic samples were firstly crushed into gravel-size chips. Clean chips were then powdered to 200 mesh for major element analysis. Measurements of whole-rock major elements were performed by using a Thermo Scientific ARL 9900 XRF. The measured values of diverse rock reference materials (BHVO-2 and BCR-2) indicate that the uncertainties are less than ±3% for elements Si, Ti, Al, Fe, Mn, Mg, Ca, K and P and less than ±6% for Na.

Trace element concentrations of Pilbara ultramafic samples were acquired using an Agilent 7700 inductively coupled plasma mass spectrometer (ICP-MS) in the Peter Hooper GeoAnalytical Laboratory at Washington State University. Sample preparation, analytical conditions, and precisions/accuracy of the analyses can be found in detail in Knaack et al. (1994). Trace element contents of Isua ultramafic samples were obtained at the University of Leeds, the U.K. These Isua ultramafic samples were first crushed into powders with a ball mill. Details of sample preparation, analytical procedures, and precisions are as follows. First, whole-rock major elements were obtained using a Thermo Scientific ARL 9900 X-ray fluorescence spectrometer. The measured values of rock reference materials BHVO-2 and BCR-2 indicate that the uncertainties on major element abundances are less than ±3 % for Si, Ti, Al, Fe, Mn, Mg, Ca, K, and P and less than ±6 % for Na. Second, for trace element analyses, about 100 μg sample powders and the reference materials BHVO-1 and JP1 were digested and dissolved with HNO_3, HCl and/or HF and diluted with ultrapure water to give a 1000-fold dilution in 3% HNO_3. Samples were analyzed for their trace element content (Sc, Ti, V, Cr, Mn, Co, Ni, Cu, Sr, Ba, Th, U, Zr, Rb, and rare earth elements) using a Thermo Scientific ICapQc ICP–MS at the University of Leeds. All concentrations were corrected for uncertainties associated with weighing and diluting the samples to produce a 1000-fold dilution. Reproducibility of the BHVO-1 reference material during the analyses was ± 6 % for the rare earth elements, and better than ± 15 % for all other elements, with the exception of V and Th (± 16 and 18 %, respectively). Reproduction of transition metal concentrations in JP1 was better than 10 relative % for all elements (Sr, Ba, Th, U, and the rare earth elements were below the detection limit of the instrument).

The major element contents of spinel crystals in Pilbara ultramafic samples were obtained in situ from petrographic thin sections using a JEOL JXA8230 Electron Probe Microanalyser (EMPA) at the University of Leeds, U.K. Major element mineral (e.g., olivine, spinel, and serpentine) compositions of the Isua ultramafic samples were analyzed in situ on petrographic thin sections by a JEOL JX8100 Electron Probe Microanalyser at the Guangzhou Institute of Geochemistry, Chinese Academy of Sciences. At the same facility, a Carl Zeiss SUPRA55SAPPHIR Field Emission Scanning Electron Microscope was used to collect images of the Isua ultramafic samples.

The HSE concentrations and Re–Os isotopic data were obtained at the Institute of Geology of the Czech Academy of Sciences, Czech Republic, using the methods detailed in Topuz et al. (2018). In brief, the samples were dissolved and equilibrated with mixed ^{185}Re-^{190}Os and ^{191}Ir–^{99}Ru–^{105}Pd–^{194}Pt spikes using Carius Tubes (Shirey and Walker, 1995) and reverse aqua regia (9 ml) for at least 72 hours. Decomposition was followed by Os separation through solvent extraction by $CHCl_3$ (Cohen and Waters, 1996) and Os microdistillation (Birck et al., 1997). Iridium, Ru, Pt, Pd, and Re were separated from the remaining solution using anion exchange chromatography and then analyzed using a sector field ICP-MS Element 2 (Thermo) coupled with Aridus II™ (CETAC) desolvating nebulizer. The isotopic fractionation was corrected using a linear law and standard Ir, Ru, Pd, Pt (E-pond), and Re (NIST 3143) solutions that were run with samples. In-run precision of measured isotopic ratios was always better than ±0.4% (2 σ). Os concentrations and isotopic ratios were obtained using negative thermal ionization mass spectrometry (Creaser et al., 1991; Völkening et al., 1991). Samples were loaded with concentrated HBr onto Pt filaments with $Ba(OH)_2$ activator and analyzed as OsO_3^- using a Thermo Triton thermal ionization spectrometer with Faraday cups in dynamic mode, or using a secondary electron multiplier in a peak hopping mode for samples with low Os concentrations. Internal precision for $^{187}Os/^{188}Os$ determination was always equal to or better than ±0.2% (2 σ). The measured Os isotopic ratios were corrected offline for oxygen isobaric interferences, spike contribution and instrumental mass fractionation using $^{192}Os/^{188}Os$ = 3.08271 (Shirey and Walker, 1998).

Literature data of Isua ultramafic rocks, crustal cumulates, and mantle peridotites are compiled for comparison (see figure captions for data sources). Fe contents of all complied data were recalculated to represent FeOt using the procedure in Gale et al. (2013). Results were plotted with GCDKit freeware developed by Janoušek et al. (2006).

4. Results

4.1. Petrographic observations

We performed thin section petrographic analysis of both Isua and Pilbara ultramafic samples to observe rock microtextures and mineral assemblages that reflect igneous and metamorphic signatures, insofar as these signatures are not obscured by alteration. Isua ultramafic samples show varying degrees of alteration (**Fig. 2, Fig. S1**). Samples AW17724-1, AW17724-4, and AW17725-2B are dominated by serpentine, magnetite and carbonate minerals. Olivine, pyroxene, or protolith textures can not be observed in these samples (**Fig. 2b, 2d, Fig. S1**). Olivine grains are preserved in three samples (i.e., AW17724-2C from lens B, AW17725-4 from lens B and AW17806-1; **Fig. 2a, 2c**). In sample AW17724-2C, Ti-humite phases (Ti-Clinohumite/Ti-Chondrodite) are found as coexisting with olivine, serpentine and magnesite. In addition, Ti-humite phases also occur as individual grains in the matrix. Magnesite is sporadically found with Ti-humite phases and olivine (**Fig. 2a**). Although some Ti-humite, magnesite and magnetite occur as apparent inclusions in olivine of AW17724-2C, they are typically associated with cracks facilitating effective element exchange between the central part of the olivine and the matrix (**Fig. 2a**). Notably, sample AW17724-2C also preserves a minor volume of talc. Retrograde alteration in this sample is characterized by younger lepidoblastic serpentine minerals cross-cutting or overgrowing olivine, Ti-humite and magnesite (**Fig. 2a**). In contrast, olivine-bearing samples AW17725-4 and AW17806-1 do not exhibit any Ti-humite phases. In addition to serpentinization, AW17725-4 shows evidence of talc alteration, whereas sample AW17806-1 equally records tremolite as an alteration product (**Fig. 2c**). Relict olivine grains preserved in sample AW17725-4 show polygonal textures, but the protolith textures of AW17806-1 are altered beyond recognition (**Fig. 2b, 2d)**.

In contrast to Isua samples, Pilbara samples have experienced complete serpentinization and minor carbonation, such that no primary ferromagnesian silicates can be identified (**Fig. 3a–c, Fig. S2**). In all Pilbara samples, serpentine grains form clusters that show similar extinction. Many such clusters have quasi-equant granular outlines. We interpret these serpentine clusters to be pseudomorphs after olivine. The interstitial space between the olivine-shaped clusters is occupied by chlorites and/or Fe-Cr-Ti oxide minerals (**Fig. 3a–b**) or serpentine (**Fig. 3a–c**). The olivine-shaped serpentine clusters appear to form self-supporting structures. Some interstitial serpentine clusters appear to preserve two pairs of relict cleavages at ~90°, indicating a pyroxene precursor (**Fig. 3a**). Some interstitial serpentine clusters are larger than the olivine-shaped serpentine clusters and enclose many of the latter grains (illustrated in **Fig. 3c**: two sets of serpentine clusters can be recognized via different brightness due to extinction). Such patterns resemble poikilitic textures in which early-formed chadacrysts are surrounded by younger, large oikocrysts (Johannsen, 1931). In some locations, the olivine-shaped serpentine clusters are compacted, forming polygonal textures (**Fig. 3c**). Late-stage alterations veins/cracks can be seen in samples AW52514-4A and AL52614-4A (**Fig. 3b**).

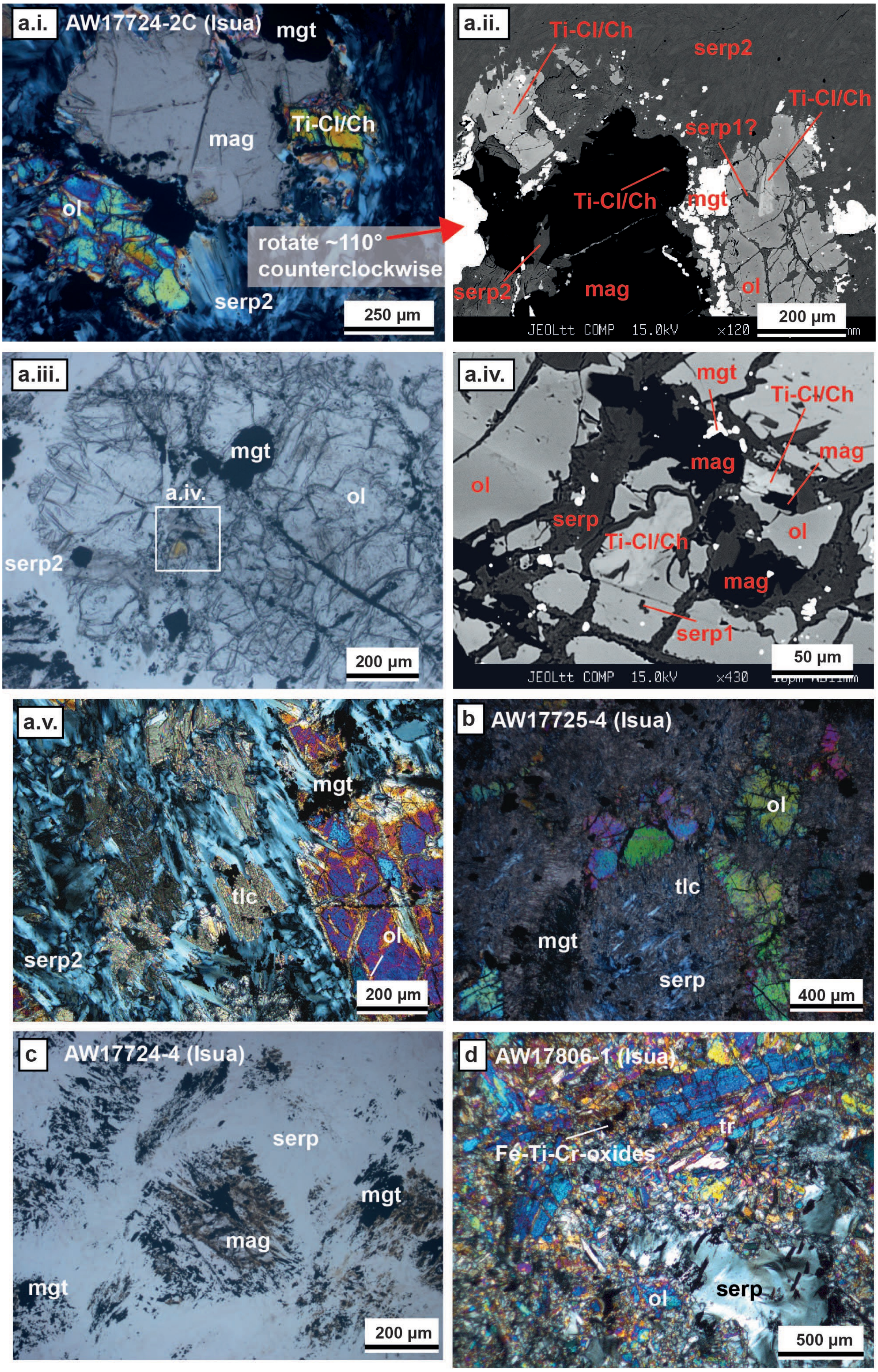

a.i. AW17724-2C (Isua)
mgt
Ti-Cl/Ch
mag
ol
rotate ~110° counterclockwise
serp2
250 µm
a.ii.
Ti-Cl/Ch
serp2
Ti-Cl/Ch
serp1?
Ti-Cl/Ch
mgt
serp2
mag
ol
200 µm
JEOLtt COMP 15.0kV x120
a.iii.
mgt
a.iv.
ol
serp2
200 µm
a.iv.
mgt
Ti-Cl/Ch
mag
mag
ol
serp
Ti-Cl/Ch
ol
mag
serp1
50 µm
JEOLtt COMP 15.0kV x430
a.v.
mgt
tlc
ol
serp2
200 µm
b AW17725-4 (Isua)
ol
tlc
mgt
serp
400 µm
c AW17724-4 (Isua)
serp
mgt
mag
mgt
200 µm
d AW17806-1 (Isua)
tr
Fe-Ti-Cr-oxides
ol
serp
500 µm

Figure 2. Representative thin section microphotographs and scanning electron microscopic images of samples from the Isua supracrustal belt. **a:** Sample AW17724-2C preserves primary olivine grains (**i** and **ii**). Two generations of serpentine minerals are identified: early-stage serpentine minerals (serp1) occur as inclusions in the olivine grains (**ii** and **iv**), and late-stage serpentine minerals (serp2) occur as lepidoblastic assemblages in the matrix cutting olivine, magnesite, and Ti-humite (**i–iv**). Both magnesite and Ti-humite are found in the matrix (**i** and **ii**) and inside the olivine grains (**iii–iv**). Due to the observed alteration including talc-alteration and serpentinization, primary igneous textures of this sample cannot be identified (**i** and **v**). **b:** Local preservation of polygonal textures by olivine grains in sample AW17725-4. **c–d:** Loss of most primary ultramafic silicates and rock textures of some Isua samples due to strong alteration (e.g., serpentinization, talc alteration, and/or amphibolite facies metamorphism). Mineral abbreviations: mag: magnesite; mgt: magnetite; ol: olivine; serp: serpentine; tlc: talc; Ti-cl: Titano-clinohumite; Ti-ch: Titano-chondrodite; tr: tremolite.

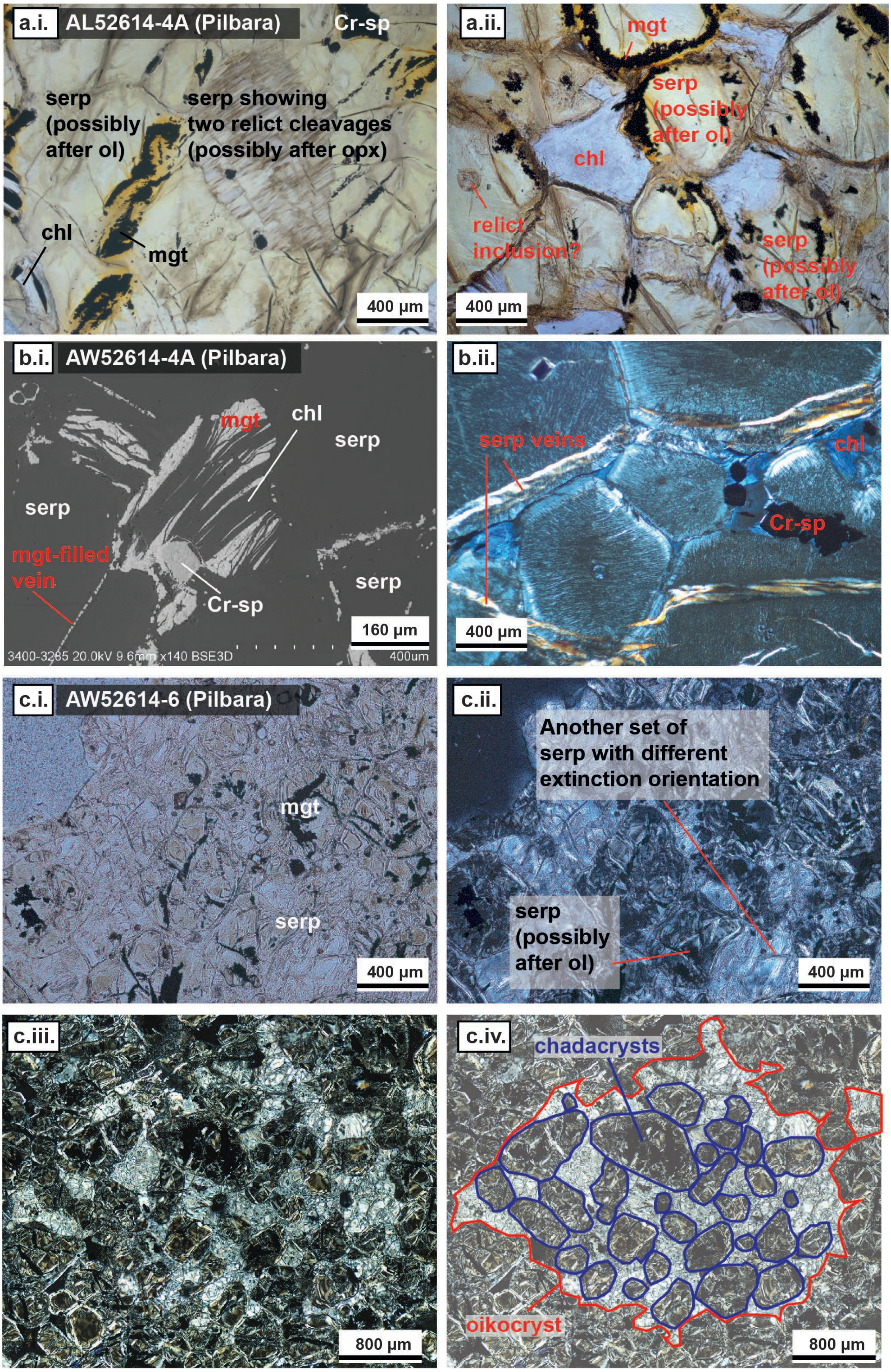
a.i.
AL52614-4A (Pilbara)
Cr-sp
serp (possibly after ol)
serp showing two relict cleavages (possibly after opx)
chl
mgt
400 µm
a.ii.
mgt
serp (possibly after ol)
chl
relict inclusion?
serp (possibly after ol)
400 µm
b.i.
AW52614-4A (Pilbara)
mgt
chl
serp
serp
mgt-filled vein
Cr-sp
serp
160 µm
3400-3285 20.0kV 9.6mm x140 BSE3D
400um
b.ii.
serp veins
chl
Cr-sp
400 µm
c.i.
AW52614-6 (Pilbara)
mgt
serp
400 µm
c.ii.
Another set of serp with different extinction orientation
serp (possibly after ol)
400 µm
c.iii.
800 µm
c.iv.
chadacrysts
oikocryst
800 µm

Figure 3. Representative thin section microphotographs and scanning electron microscopic images of samples from the East Pilbara Terrane. Pilbara samples show complete serpentinization, yet their primary rock textures are preserved by serpentine pseudomorphs. **a:** Sample AW52614-4A shows compacted olivine-shaped serpentine clusters (**ii**) which locally form polygonal textures (featured by abundant 120° triple junctions). **b:** Alteration minerals such as chlorite, serpentine and magnetite occur in interstitial spaces **(i)** and veins in sample AW52614-4A **(ii)**. In **c.ii**, **c.iii** and **c.iv**, two sets of serpentine clusters are recognized with the cross-polarized light photomicrographs. One set shows black/dark grey color, with outlines similar to olivine grains. Another set is in white/light grey, which appears to enclose the serpentine clusters of the first set. This texture resembles cumulate textures, where smaller chadacrysts could be included in larger oikocrysts. Mineral abbreviations: chl: chlorite; Cr-sp: Cr-spinel; mag: magnesite; mgt: magnetite; ol: olivine; opx: orthopyroxene; serp: serpentine;

Table 1: Mineralogy and location information of investigated samples.

Sample ID	GPS coordinates (WGS84 datum)	Location/Unit	Mineralogy
The Isua supracrustal belt			
AW17724-1	65.153681 N, 50.143989 W	Serpentinite layer enveloping the meta-peridotite lens B in the western belt	serpentine+talc+magnetite
AW17724-2C	65.153974 N, 50.144801 W	The meta-peridotite lens B in the western belt	olivine+serpentine+magnetite±Ti-humite±magnesite±talc
AW17724-4	65.156859 N, 50.143249 W	The meta-peridotite lens B in the western belt	serpentine+magnetite+magnesite±talc
AW17725-2B	65.154857 N, 50.138543 W	~300 meters east of lens B in the western belt	carbonate+magnetite±serpentine
AW17725-4	65.139544 N, 50.149716 W	The meta-peridotite lens A in the western belt	serpentine+talc+olivine±magnetite
AW17806-1	65.191627 N, 49.840547 W	An outcrop in the eastern belt near the north tonalite	olivine+pyroxene+tremolite ±serpentine±Fe-Ti-Cr oxides
The East Pilbara Terrane			
AW52614-4A	20.917983 S, 119.982300 E	The Gap Intrusion	serpentine+Fe-Ti-Cr oxides+chlorite±apatite
AL52614-4A	20.917983 S, 119.982300 E	The Gap Intrusion	serpentine+Fe-Ti-Cr oxides+chlorite
AW52614-6	20.930950 S, 119.867500 E	The Gap Intrusion	serpentine+Fe-Ti-Cr oxides+chlorite

4.2. Whole-rock major and trace element characteristics

Whole-rock major and trace element characteristics are often used to indicate the petrogenetic conditions, such as the degree of melt depletion, and the sources of ultramafic rocks (e.g., Niu and Hekinian, 1997; Van de Löcht et al., 2020), although effects of alteration (as observed in section 4.1) must be considered. Isua ultramafic rocks have SiO_2 of ~38–49 wt.%, MgO of ~31–47 wt.%, CaO of ~0.03–10.49 wt.%, Al_2O_3 of ~0.5–5.0 wt.%, FeOt of ~6.2–10.7 wt.%, Mg# [i.e., Mg/(Mg+Fe)] of 84–93, and loss-on-ignition (LOI) of ~5–21 wt.% (all major oxide concentrations are anhydrous values, i.e., normalized to zero LOI and 100 wt.% total; **Figs. 4–6, Table S1**). For trace element results (**Fig. 7**), we excluded those that were not reproduced by measurements on reference materials (e.g., Nb and Ta for Isua ultramafic samples). The trace element abundances of Isua ultramafic samples are mostly 0.1–10 times those in the modelled primitive mantle (McDonough and Sun, 1995; same below; **Fig. 7**). These samples show a fractionation trend from light to medium rare earth elements with $(La/Sm)_{PM}$ values ranging from ~1.5–3.8 (i.e., the ratio of concentrations that have been normalized to those of the primitive mantle) (**Fig. 7a, 7c**). The heavy rare earth elements of Isua ultramafic samples indicate a flat trend or variably fractionated trends with $(Dy/Yb)_{PM}$ of ~0.3–1.2 (**Fig. 7a**). The Th concentrations and Dy/Yb ratios (proxies for alterations; **Fig. 7b**; Deschamps et al., 2013) of Isua ultramafic samples range from 0.04–0.13 ppm and 0.5–1.9, respectively.

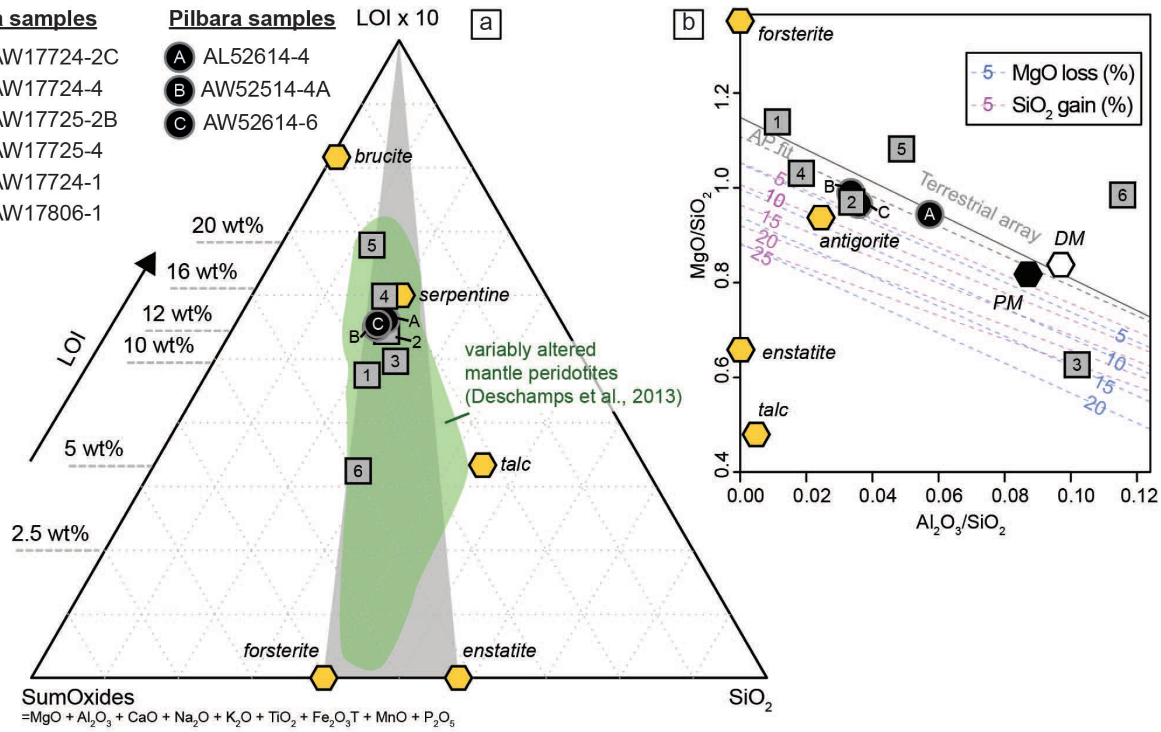

Figure 4. Major element and loss-on-ignition (LOI) geochemical characteristics of Pilbara and Isua ultramafic samples in comparison with common primary and alteration minerals in ultramafic rocks. All major element concentrations are anhydrous values (i.e., normalized to zero LOI and 100 wt.% total). Panel **a** shows a ternary plot of SiO_2, LOI, and SumOxides (MgO + Al_2O_3 + CaO + Na_2O

+ K_2O + TiO_2 + Fe_2O_3T + MnO + P_2O_5) (modified from Deschamps et al., 2013). Panel **b** shows MgO/SiO_2–Al_2O_3/SiO_2 space with Pilbara and Isua ultramafic samples, common primary and alteration minerals in ultramafic rocks, the terrestrial array of mantle peridotites (fitted by abyssal peridotites, AP), and MgO-loss or SiO_2-gain alteration curves. The data in this figure show that the major element systematics of our Isua and Pilbara samples reflect various degrees of serpentinization without strong talc alteration, consistent with thin-section petrography (**Figs. 2–3**). Two samples (AW17725-2B, AW17806-1) which were collected from outcrops near the meta-tonalite have significantly elevated Al_2O_3. These high Al concentrations cannot be attributed to serpentinization and talc alteration. Panel b is modified from Malvoisin et al. (2015) which itself is a modified version of Jagoutz (1979). PM: primitive mantle; DM: depleted mantle. All mantle values are from McDonough and Sun (1995).

Pilbara ultramafic rocks have whole-rock SiO_2 of ~43–46 wt.%, MgO of ~41–45 wt.%, CaO of 0.02–0.12 wt.%, Al_2O_3 of ~1.6–2.5 wt.%, FeOt of ~6.1–12.8 wt.%, Mg# of 85–93, and LOI of 12.3–12.9 wt.% (**Figs. 4–6, Table S1).** The trace element abundances in these samples are also 0.1–10 times those in the modelled primitive mantle. Pilbara samples show fractionated light to medium rare earth elements, with $(La/Sm)_{PM}$ ranging from 1.9 to 2.4 (**Fig. 7**). These samples also have weak negative Nb anomalies, and generally flat heavy rare earth element trends [with $(Dy/Yb)_{PM}$ of 0.8–1.1]. The Th concentrations and Dy/Yb ratios of Pilbara ultramafic samples range from 0.10 to 0.19 ppm and 1.2–1.7, respectively (**Fig. 7b**). The PM-normalized (Becker et al., 2006) HSE patterns of the Pilbara samples exhibit similar fractionated patterns characterized by Os–Ir depletion over Ru [$(Ru/Ir)_{PM}$ = 2.0–3.5] and Pt depletion over Os-Ir [$(Pt/Ir)_{PM}$ =0.3–0.6], whereas Pd and Re contents are highly variable (**Fig. 8**). One Pilbara sample (AW52514-4A) shows significantly higher Pd abundance (close to the primitive mantle value) than the rest of the samples. The present-day $^{187}Os/^{188}Os$ values range between ~0.1094 and 0.1166. Rhenium contents are high in two samples (0.13 ppb in AL52614 and 0.35 ppb in AW52514), resulting in superchondritic $^{187}Re/^{188}Os$ (0.53 and 0.86, respectively) and together with unrealistic low initial $^{187}Os/^{188}Os$ values (<0.078) calculated at ~3.4 Ga.

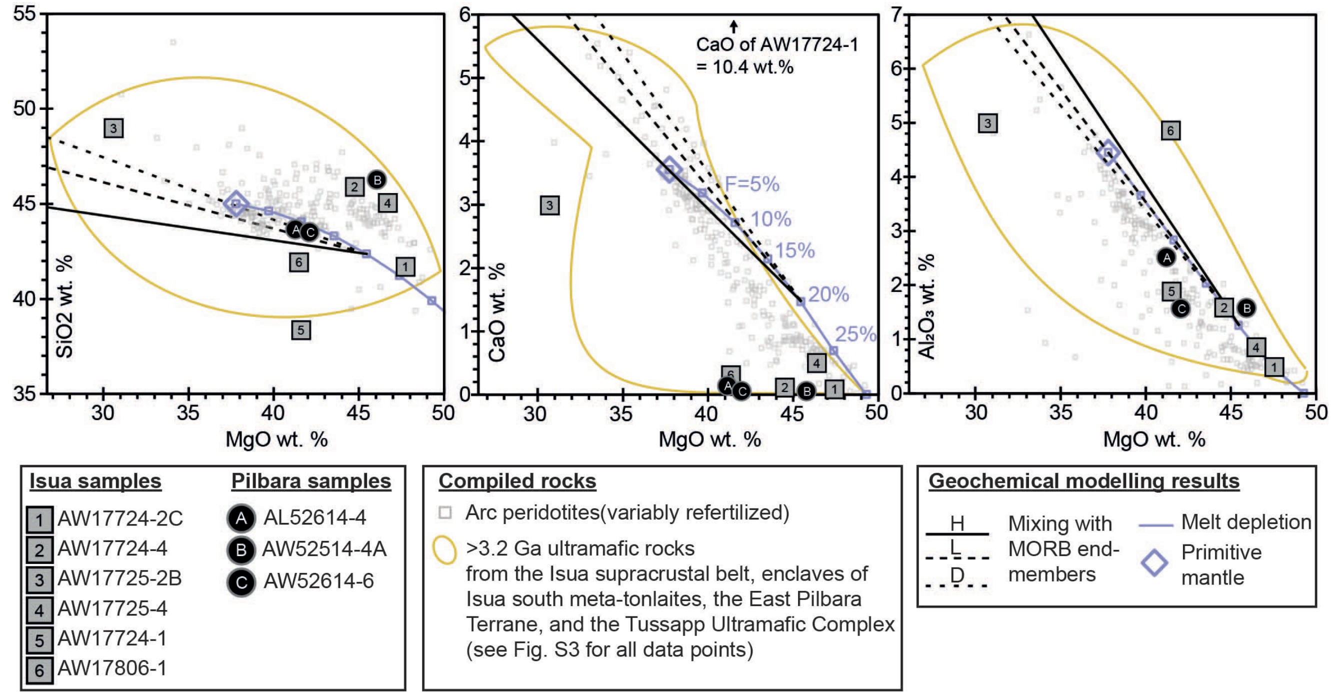

Figure 5. Major element abundances versus Mg# of Pilbara and Isua ultramafic samples. Geochemistry of arc peridotites, other compiled >3.2 Ga ultramafic rocks from the Isua and Pilbara areas, and MELTS modelling results are also plotted for comparison. References of compiled >3.2-Ga ultramafic rocks are listed in the **Fig. 1** caption. All data are presented using anhydrous values (i.e., all major element abundances are normalized to zero LOI and 100 wt.% total). Data for arc peridotites are from Chin et al. (2014) and references therein. Primitive mantle values are from McDonough and Sun (1995). The mixing lines represent mixing between 20% depleted primitive mantle and mid-ocean ridge basalt (MORB) end-members H, L, and D (Elthon, 1992). Details of MELTS modelling are in Chin et al. (2014). Data sources: Serpentinites from the Nob Well Intrusion of the East Pilbara Terrane: Geological Survey of Western Australia 2013 database. Compiled ultramafic rocks from the Isua supracrustal belt: Friend and Nutman (2011); Szilas et al. (2015). Compiled ultramafic rocks from enclaves in meta-tonalite south of the Isua supracrustal belt: Friend et al. (2002); Van de Löcht et al. (2020). Ultramafic rocks from the Tussapp Ultramafic Complex: McIntyre et al. (2019).

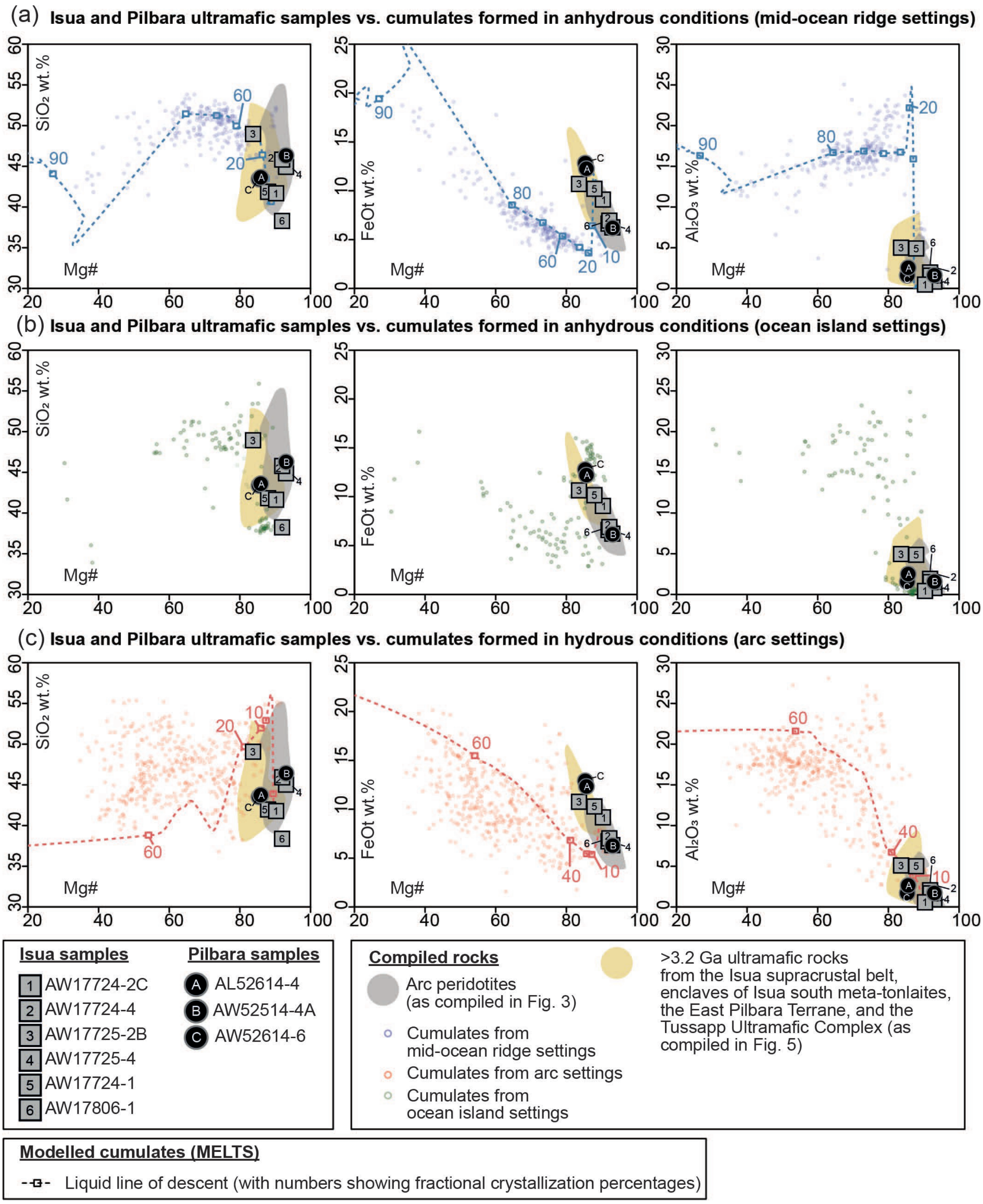

Figure 6. Major element geochemical characteristics of the Isua and Pilbara ultramafic samples in comparison with those of Phanerozoic cumulates, arc peridotites, >3.2 Ga ultramafic rocks (see **Fig. 3** for data sources), and modelled liquid lines of descent. All data are presented using anhydrous values (i.e., all major element abundances are normalized to zero LOI and 100 wt.% total). The data in this figure show that Isua and Pilbara ultramafic rocks, Mg-rich cumulates and mantle peridotites have similar major element geochemical systematics. Data

sources for the cumulates and MELTS modelling curves are from Chin et al. (2018), Mallik et al. (2020), and references therein.

4.3. Mineral geochemistry

Olivine grains in Isua sample AW17724-2C (lens B) have extraordinarily high Mg# values of ~95–98 and NiO of ~0.39–0.63 wt.%. In contrast, olivine grains in Isua sample AW17725-4 (lens A) have Mg# values of ~87 and NiO of ~0.52–0.61 wt% (**Table S2**). Ti-humite phases in sample AW17724-2C have variable TiO_2 abundances of ~3.0–8.1 wt.%. All analyzed spinel grains in the Isua samples contain a high magnetite component (i.e., FeOt of ~90 wt.%) (**Table S2**).

Spinel crystals of both chromite or magnetite compositions occur in the Pilbara samples. Specifically, chromite spinel grains have Cr_2O_3 of ~40–50 wt.%, TiO_2 of 0.6–4.3 wt.%, and MgO of 5–12 wt.%. The Cr# [Cr/(Cr+Al)] values and Mg# values of chromite spinel grains are ~65–75 and ~17–46, respectively (**Fig. 9**; **Table S2**).

5. Discussion

We analyzed phaneritic ultramafic rocks in the Eoarchean Isua supracrustal belt and the East Pilbara Terrane to explore their petrogenesis as a means of testing the viability of existing tectonic models. Specifically, we explore whether these rocks need to be explained as mantle peridotites that emplaced in the crust in a subduction setting. Our new petrological and geochemical data from six ultramafic samples from the Isua supracrustal belt and three ultramafic samples from the East Pilbara Terrane show that (1) Isua and Pilbara samples have been variably altered and now contain several alteration minerals (e.g., serpentine, talc, carbonate) that replaced igneous ferromagnesian silicates; (2) Ti-humite phases preserved in one Isua ultramafic sample (AW17724-2C from lens B) appear to be in close association with magnesite + olivine + talc + serpentine (**Fig. 2**); (3) Pilbara ultramafic samples preserve poikilitic textures and polygonal textures (**Fig. 3**); one Isua sample (AW17725-4 from lens A) also preserves relict polygonal textures; (4) trace element abundances in both Isua and Pilbara ultramafic samples range from the highly depleted, with respect to the PM values (0.1 times PM values), to highly enriched (10 times PM values) (**Fig. 6a–b**); (5) two out of three Pilbara ultramafic samples show fractionated, relatively high concentrations of Os and Ir versus Pt, Pd, and Re in the PM-normalized diagram (**Fig. 7c**); and (6) chromite spinel in Pilbara ultramafic samples feature Cr# of ~65–75, and Mg# of ~17–46 (**Fig. 9**). In the following sections, we first discuss the potential impacts of alterations on petrology and geochemistry. Then, we show that new and compiled petrology, geochemistry, and microstructures of Isua and Pilbara ultramafic rocks are consistent with a cumulate origin, whereas an origin as thrust-emplaced mantle slices is not required. We then discuss the implications for testing early Earth tectonic models and the initiation of plate tectonics.

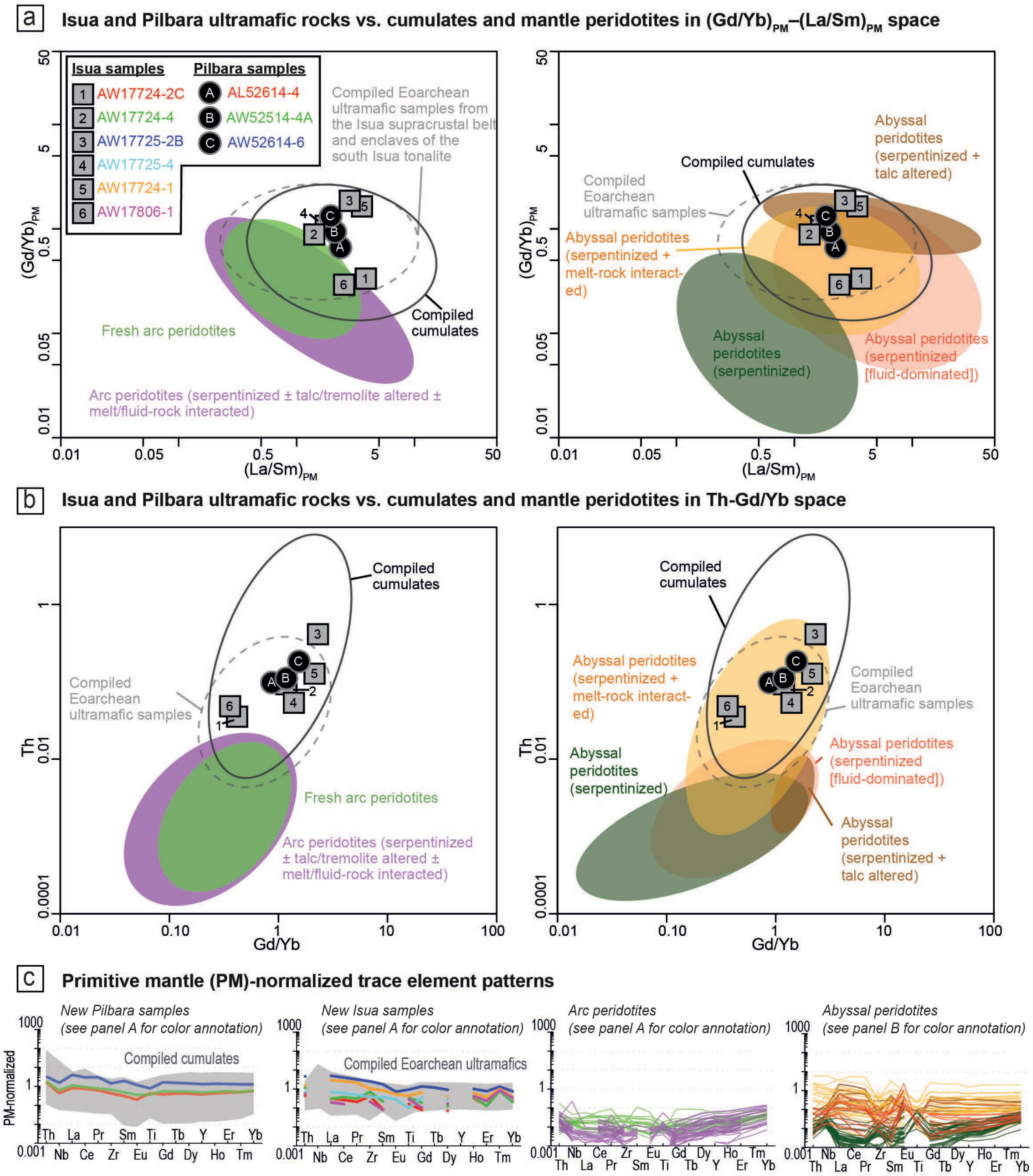

Figure 7. Trace element characteristics for Isua and Pilbara ultramafic samples in comparison with compiled cumulates and variably altered mantle peridotites. **a**, Primitive mantle (PM) normalized Gd/Yb and La/Sm ratios [i.e., $(Gd/Yb)_{PM}$ and $(La/Sm)_{PM}$] of investigated samples and compiled rocks. **b**, Th and Gd/Yb ratios of investigated samples and compiled rocks. **c**, PM-normalized spider diagrams showing trace element patterns of investigated samples and compiled rocks (see **Figure S4** for spider diagrams with sample locations). These diagrams show that new and compiled data for ultramafic rocks from the Isua supracrustal belt have similar trace element characteristics to dunite enclaves from the south Isua meta-tonalites, Pilbara ultramafic samples and ultramafic cumulates. Only some abyssal peridotites which experienced serpentinization and melt-rock interactions have comparable trace element patterns. Other mantle peridotites have lower Th, Gd/Yb, $(Gd/Yb)_{PM}$, and/or $(La/Sm)_{PM}$ values. Data sources: compiled cumulates involve samples from the Permian Lubei intrusion of NW China (Chen et a., 2018), the late Proterozoic Ntaka Ultramafic Complex of Tanzania (Barnes et al., 2016), the Mesoarchean Nuasahi Massif of India (Khatun et al., 2014), the Mesoarchean Tartoq Group of SW Greenland (Szilas et al., 2014), the Mesoarchean Seqi Ultramafic Complex of SW Greenland (Szilas et al., 2018), and the Eoarchean Tussapp Ultramafic Complex of SW Greenland (McIntyre et al., 2019); compiled Eoarchean ultramafic samples are rocks from the Isua supracrustal belt (Szilas et al., 2015) and the enclaves in meta-tonalite south of the Isua supracrustal belt (Van de Löcht et al., 2020); fresh arc peridotites are from the Kamchatka arc (Ionov, 2010); arc peridotites that experienced serpentnization, talc/tremolite alteration, and/or melt-rock interactions are from the Loma Caribe peridotite body of Dominican Republic (Marchesi et al., 2016) and the Izu-Bonin-Mariana forearc (Parkinson and Pearce, 1998); abyssal peridotites that experienced serpentinization are from the Oman ophiolite (Hanghøj et al., 2010); variably altered abyssal peridotites from the Mid-Atlantic Ridge are summarized by Paulick et al. (2006). Primitive mantle values are from McDonough and Sun (1995).

5.1. Assessment of alteration impacts

Petrological and geochemical information obtained from Isua and Pilbara ultramafic rocks represents the combined effects of petrogenetic processes and alterations. Below we discuss potential types and impacts of alteration on the petrology and geochemistry of these rocks.

High-grade (e.g., granulite facies) metamorphism can lead to partial melting. The partial melting process and subsequent melt-rock interactions could strongly disturb the geochemistry and mineral assemblages of affected rocks. However, the Isua supracrustal belt and the area from which Pilbara ultramafic samples were collected (**Fig. 1**) have only experienced amphibolite facies metamorphism (or lower conditions) (e.g., Hickman, 2021;

Ramírez-Salazar et al., 2021). In general, for an anhydrous system larger than a hand specimen, amphibolite facies or lower metamorphism is usually considered isochemical. However, both Isua and Pilbara samples show evidence of hydrothermal alterations, as indicated by the dominance of serpentine minerals (**Figs. 2–3**). Therefore, some whole-rock geochemical changes are possible (see below). In addition, at mineral scales, some chemical changes during metamorphism are possible. For example, Cr-spinel could be altered to magnetite during metamorphism (e.g., Barnes and Roeder, 2001). Therefore, care must be taken when interpreting petrogenesis using spinel data.

Fluid assisted alterations could result in changes in mineral assemblages and element concentrations, especially for fluid-mobile elements (e.g., K, Ca, Si, Rb, Ba and Sr, etc.). LOI contents (**Fig. 4a**), and the presence of serpentine, talc, and/or magnesite (**Figs. 2–3**) in Isua and Pilbara ultramafic samples show that these rocks have experienced variable degrees of serpentinization and carbonitization (including talc -alteration; although some magnesite crystals could be primary minerals crystallized from fluid-rich magmas, see **Fig. 2a** for magnesite crystals as olivine inclusions; also Smithies et al., 2021). A ternary plot of anhydrous SiO_2, LOI, and other oxides (e.g., MgO, TiO_2, see **Fig. 4** caption) shows that serpentinization is the dominant controlling factor for their geochemistry as these samples plot near the serpentine mineral composition. Effects of other alterations on major element concentrations and LOI (e.g., Deschamps et al., 2013; Paulick et al., 2006) in most samples seem to be secondary with the exception of sample AW17724-1 which has a high anhydrous CaO concentration (10.4 wt.%). Hydrothermal fluids may mobilize some elements such as Mg, Si, and trace elements including REEs (e.g., Deschamps et al., 2013; Malvoisin et al., 2015; Paulick et al., 2006). Nonetheless, the potential MgO and SiO_2 loss/gain could be insignificant (i.e., $<10\%$) compared to other factors (e.g., melt depletion, melt-rock interaction, or talc-alteration, see **Fig. 4b**; Snow and Dick, 1995). Some HSEs like Os, Ir, Ru and Pt are largely immobile during fluid assisted alterations, but Pd and Re could be mobile (e.g., Büchl et al., 2002; Deschamps et al., 2013). Spinel Al and Cr concentrations can be increased or reduced during fluid-rock interaction, respectively (e.g., El Dien et al., 2019).

Melt-rock interaction is commonly observed in mantle rocks (e.g., Ackerman et al., 2009; Büchl et al., 2002; Deschamps et al., 2013; Niu, 2004; Paulick et al., 2006) where ascending melts react with wall rocks. This process is similar to reactions between cumulate phases and trapped/evolving melts during crystallization or post-cumulus processes (e.g., Borghini and Rampone, 2007; Goodrich et al., 2001; Wager and Brown, 1967). In general, melt-rock interaction can alter the geochemistry of affected rocks towards those of melts at increasing rock/melt ratios (e.g., Kelemen et al., 1992; Paulick et al., 2006). For peridotites interacting with basalts or more evolved melts, the elevation of elements that are relatively enriched in melts (e.g., Si, Ca, Th, Al, Fe, Ti, LREE, Pt, Pd, and Re) is significant (**Figs. 4–7**; e.g., Deschamps et al., 2013; Hanghøj et al., 2010). Other effects include changes in mineral modes and/or mineral geochemistries (e.g., olivine Mg# reduction; spinel Cr-loss and Al-gain) (e.g., El Dien et al., 2019; Niu and Hekinian, 1997). Two Isua supracrustal belt ultramafic samples (AW17725-2B, AW17806-1) which were sampled near the meta-tonalite bodies have the highest Al_2O_3 and lowest MgO concentrations among all samples (**Figs. 4b, 5**), which may be explained by reactions with relatively Al_2O_3 rich components (fluids and/or melts).

In summary, fluid/melt rock interaction might partly control the observed geochemistry and petrology of studied Isua and Pilbara samples. Therefore, for petrogenetic interpretation, we compare the observed geochemistry and petrology of Isua and Pilbara ultramafic samples with those of cumulates and mantle peridotites that potentially experienced similar alterations (including serpentinization, talc/tremolite alteration, and melt-rock interaction).

5.2. Isua and Pilbara ultramafic rocks, similar or different?

Ultramafic rocks from the East Pilbara Terrane were produced by non-plate tectonic processes (Collins et al., 1998; Hickman, 2021). Therefore, a comparison between Isua and Pilbara ultramafic rocks can be used to explore the viability of non-plate tectonic models for the Isua supracrustal belt. Serpentine grains preserved in Pilbara samples (**Fig. 3**) appear to be pseudomorphs after primary olivine and pyroxene. Spinel is abundant in our Pilbara ultramafic samples (**Fig. 3**). Olivine grains preserved in the lens A sample AW17725-4 have forsterite contents of ~87, slightly lower than published forsterite contents of ~88-92 for lens A meta-dunite samples (e.g., Szilas et al., 2015; Nutman et al., 2020). These olivine grains from lens A meta-dunite samples have been interpreted as primary igneous olivine (e.g., Szilas et al., 2015; Nutman et al., 2020). Other primary minerals observed in our and compiled Isua ultramafic samples are olivine, pyroxene and spinel (**Fig. 2**; e.g., Szilas et al., 2015; Nutman et al., 2020; Van de Löcht et al., 2020;). Therefore, Isua ultramafic samples potentially have similar protolith mineral assemblages (olivine + spinel ± pyroxene) to their Pilbara counterparts. Pyroxene appears to be a minor component in Pilbara ultramafic samples and spinifex textures are not observed (**Fig. 3**), which do not support an extrusive komatiite origin for our Pilbara ultramafic samples. Instead, the poikilitic textures of Pilbara ultramafic rocks (**Fig. 3c**) as preserved by the serpentine pseudomorphs can only be explained by originating as olivine-rich cumulates (Wager and Brown, 1967). The polygonal textures of Pilbara ultramafic rocks (**Fig. 3b**) likely developed via re-equilibration and recrystallization of cumulate olivine grains under crustal conditions (e.g., Hunter, 1996). Therefore, rock textures support the hypothesis that Pilbara ultramafic samples are cumulates. However, primary rock textures of most of our Isua ultramafic samples are lost due to alteration (**Fig. 2a, 2c–d**). Only one sample (AW17725-4) from the meta-peridotite lens A preserves relict polygonal textures that feature abundant ~120° triple junctions of olivine grains (**Fig. 2b**), consistent with findings in rocks sampled from nearby outcrops (e.g., Nutman et al., 1996) and Pilbara ultramafic samples (**Fig. 3b**).

Alteration overprints observed in the Isua ultramafic rocks are different from those of Pilbara ultramafic samples. One Isua ultramafic sample from lens B (AW17724-2C) preserves Ti-humite phases that grew in equilibration with secondary highly forsteritic olivine (with Mg# of 95–98; **Table S2**), magnesite, serpentines (serp1 in **Fig. 2a**), and/or perhaps talc (**Fig. 2a**) (cf. Nutman et al., 2020; Nutman et al., 2021; Guotana et al., 2021). This was followed by additional serpentinization as reflected by serpentine minerals (serp2 in **Fig. 2a**) cross-cutting the pre-existing minerals, including olivine, magnesite and older serpentine grains (i.e., serp1) (**Fig. 2a**). Other Isua ultramafic samples show variable degrees of serpentinization and talc/tremolite alteration (**Fig. 2b–d**). In contrast, our Pilbara ultramafic samples are devoid of tremolite/talc carbonate alterations. Serpentinization occurs in Pilbara ultramafic samples but appears to be much more pervasive compared to Isua ultramafic samples (**Fig. 3**). Small (~20 μm in diameters) clinopyroxene inclusions in olivine or mantle-like olivine oxygen isotopes from Isua meta-dunite samples of lens A have been reported as evidence of melt-rock or fluid-rock alterations, respectively (Nutman et al., 2021), but the degrees of serpentinization in Pilbara samples prevented us from conducting similar analyses. Most opaque minerals in Isua ultramafic samples appear to be magnetite, whereas chromite is rare (**Fig. 2**; Nutman et al., 2021; Szilas et al., 2015). In contrast, chromite (sometimes rimmed by magnetite, **Fig. 3a-b**) is common in Pilbara samples. Some of these differences in alteration styles may result from different regional metamorphic grades such that the Isua supracrustal belt might have experienced multiple metamorphic/metasomatic events under conditions up to upper amphibolite facies (e.g., Ramírez-Salazar et al., 2021), whereas supracrustal belts of the East Pilbara Terrane predominantly experienced greenschist facies conditions (e.g., Hickman, 2021).

Weak crystallographic preferred orientations (CPOs) of olivine crystals in Isua ultramafic samples from lenses A and B match the CPO pattern created by B-type slip (via dislocation creep) that is commonly found in hydrous mantle wedge settings (Kaczmerak et al., 2016 and references therein). The alteration degrees of Pilbara ultramafic samples again inhibit us from examining their olivine CPOs. The shapes of serpentine pseudomorphs in these Pilbara ultramafic samples show that cumulate textures are relatively well preserved, with no sign of strong deformation after complete serpentinization (**Fig. 2e–g**).

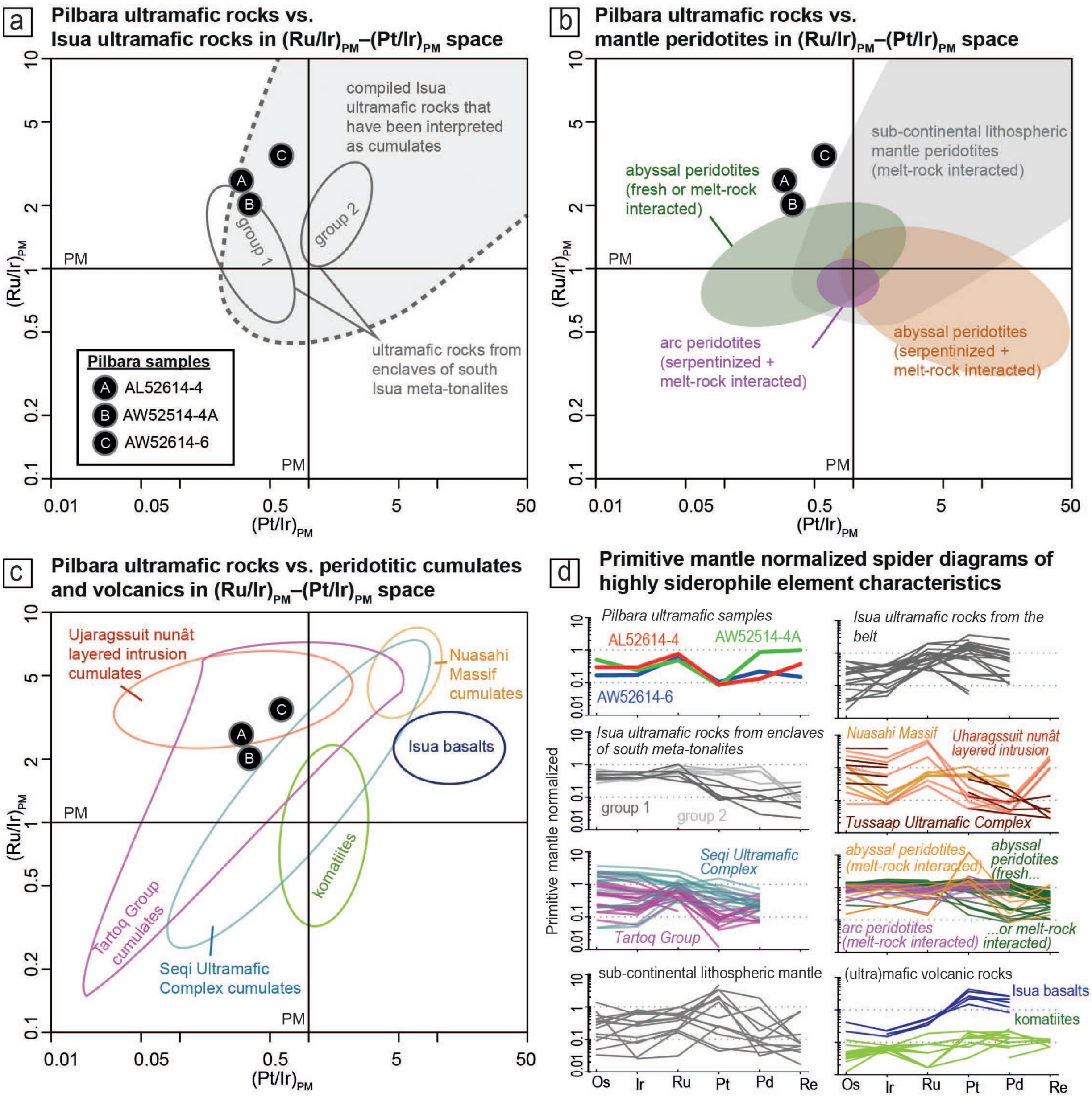

Figure 8. Highly siderophile element (HSE) (including platinum-group elements, PGEs: Os, Ir, Ru, Pt, and Pd) characteristics of the Pilbara samples, Isua ultramafic rocks, cumulates, volcanics and mantle peridotites. Panels **a** to **c** show primitive mantle (PM)-normalized Pt/Ir and Ru/Ir ratios [i.e., $(Pt/Ir)_{PM}$ and $(Ru/Ir)_{PM}$] of new Pilbara samples in comparison with those of Isua ultramafic rocks (from the supracrustal belt and peridotite enclaves, see Figure 4 caption; panel a), mantle peridotites (panel b), volcanics (komatiites and basalts) and peridotitic cumulates (panel c). Peridotites from meta-tonalite enclaves south of the Isua supracrustal belt are divided by Van de Löcht et al. (2018) into two groups according to their HSE signatures: "group 2" peridotites have higher Pt, Pd and Re versus "group 1" peridotites. Panel **d** shows PM-normalized HSE patterns of new Pilbara samples and compiled rocks in spider diagrams. These plots show that HSE characteristics of Pilbara ultramafic rocks are similar to those of cumulate rocks, but are different from those of mantle peridotites. Furthermore, HSE patterns of ultramafic rocks from peridotite enclaves of meta-tonalites south of the Isua supracrustal belt are consistent with those of cumulates and do not require mantle peridotite origins (cf. Van de Löcht et al., 2018). Data sources: compiled cumulates involve samples from the Eoarchean Uharagssuit nunât layered intrusion of southwestern Greenland (Coggon et al., 2015) the Mesoarchean Nuasahi Massif of India (Khatun et al., 2014), the Mesoarchean Tartoq Group of southwestern Greenland (Szilas et al., 2014), the Mesoarchean Seqi Ultramafic Complex of southwestern Greenland (Szilas et al., 2018), and the Eoarchean Tussapp Ultramafic Complex of southwestern Greenland (McIntyre et al., 2019); compiled Isua ultramafic samples and basalts are from the Isua supracrustal belt (Szilas et al., 2015) or the peridotite enclaves in meta-tonalite south of the Isua supracrustal belt (Van de Löcht et al., 2018); komatiites are from the Paleoarchean Barberton Greenstone Belt of South Africa (Maier et al., 2003); arc peridotites experienced serpentinization and melt-rock interaction are from the Northwest Anatolian orogenic complex, Turkey (Aldanmaz and Koprubasi, 2006); fresh and variably melt-refertilized abyssal peridotites are from the collisional massifs in Italian Alps, Italy (Wang et al., 2013); abyssal peridotites that experienced serpentnization and melt-rock interaction are from the Troodos Ophiolite Complex of Cyprus (Büchl et al., 2002); sub-continental lithospheric mantle rocks that experienced melt-rock interactions are from the Bohemian

Massif of the Czech Republic (Ackerman et al., 2009). Primitive mantle values: Becker et al. (2006).

Ultramafic samples from the Isua supracrustal belt have similar major and trace element geochemistry to the Pilbara ultramafic samples (see below; **Figs. 4–9**). Three (AW17724-2C, AW17724-4, and AW17725-4) Isua ultramafic samples from meta-peridotite lenses show similar compositions to three Pilbara ultramafic samples in MgO–SiO_2, MgO–CaO, and MgO–Al_2O_3 spaces (**Fig. 5**). Three Isua ultramafic samples collected from the Isua supracrustal belt outside of the lenses either have extraordinarily low MgO (AW17725-2B), high CaO (AW17724-1), or high Al_2O_3 (AW17725-2B and AW17806-1). Both Isua and Pilbara ultramafic samples show similar normalized trace element abundances (i.e., ~0.1–10 times PM). In PM-normalized diagrams, the Pilbara ultramafic samples show fractionated La-Sm trends [with $(La/Eu)_{PM}$ of ~1.9–2.4], and generally unfractionated heavy REE [with $(Dy/Yb)_{PM}$ of ~0.8–1.2] (**Fig. 7a**). Such fractionation trends are consistent with some Isua ultramafic samples [note that all Isua samples have $(La/Sm)_{PM}$ of ~1.5–3.8 and $(Dy/Yb)_{PM}$ of ~0.3–1.2; **Fig. 7a**]. The Th concentrations and Gd/Yb ratio are also similar (Isua versus Pilbara ultramafic rocks: ~0.04–0.13 versus ~0.10–0.19 ppm; ~0.5–1.9 versus 1.2–1.7, respectively; **Fig. 7b**).

Pilbara ultramafic samples appear to have similar HSE patterns compared to some ultramafic samples from the Isua supracrustal belt [compiled from Szilas et al. (2015); **Fig. 8a**]. All three Pilbara ultramafic samples have high PM-normalized concentrations of Os, Ir, and Ru (I-PGE) relative to Pt and positive Ru anomalies (note that Pd and Re could be mobilized during alterations, see section 5.1), highlighted by $(Pt/Ir)_{PM}$ of ~0.3–0.6 and $(Ru/Ir)_{PM}$ of ~2.0–3.5. Compiled ultramafic rocks of the Isua supracrustal belt (Szilas et al., 2015), including those from the dunite lenses, have much broader ranges of $(Pt/Ir)_{PM}$ (~0.5–26.1) and $(Ru/Ir)_{PM}$ (~0.6–18.2) values which largely encompass these of Pilbara ultramafic samples. In contrast, “group 1” peridotites from ultramafic enclaves in the meta-tonalite south of the Isua supracrustal belt (**Fig. 8a**; Van de Löcht et al., 2018) have unfractionated to slightly fractionated Os-Ir-Ru elements [with $(Ru/Ir)_{PM}$ of ~0.6–2.0] and relatively low Pt and Pd versus I-PGE [with $(Pt/Ir)_{PM}$ of ~0.2–0.5].

Spinel crystals from the Pilbara ultramafic samples show similar chemistry to those of new and compiled ultramafic samples from the Isua supracrustal belt. Our Pilbara ultramafic samples preserve both chromite and magnetite. The chromite crystals in these samples show relatively constant Cr# (~60–80), highly variable TiO_2 (~0.5–5.0 wt.%), and variable Mg# (~20–50). Only magnetite was found in our Isua ultramafic samples from the dunite lenses, which shows low TiO_2 (<0.5 wt.%), high Cr# (>90), and low Mg# (<20) (**Fig. 9**). Compiled ultramafic samples from the dunite lenses of the Isua supracrustal belt contain both chromite and magnetite (Szilas et al., 2015). Most of the compiled chromite from these samples shows similar Mg# and Cr# values to the chromite from the Pilbara samples. Other chromite yields Mg# and Cr# trends towards the magnetite composition (**Fig. 9**). The compiled chromite also shows variable TiO_2 (~0.2–2.4 wt.%).

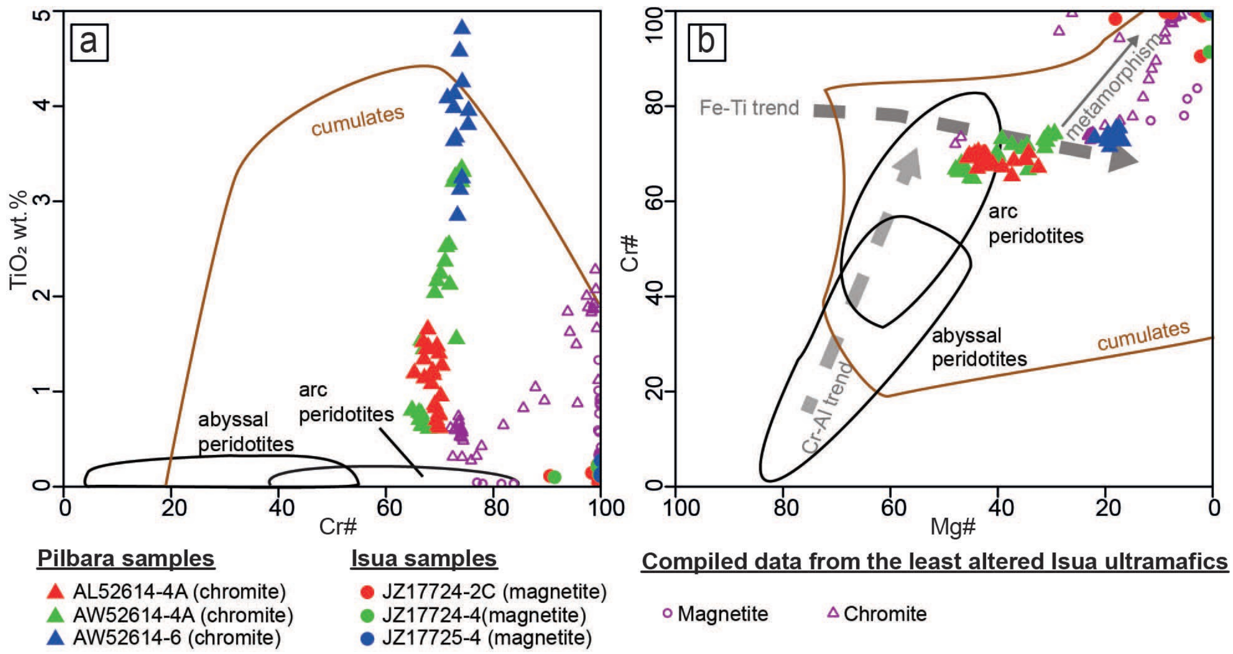

Figure 9. Geochemical signatures of spinel in Pilbara and Isua samples, plotted with compiled fields for ultramafic cumulates and mantle peridotites. Panel **a** shows Cr# values [Cr/(Cr+Al)] and TiO_2 concentrations of spinel. Panel **b** shows Mg# [Mg/(Mg+Fe)] and Cr# values of spinel. The Fe–Ti trend of spinel (representing equilibration during fractional crystallization) and the Cr–Al trend of spinel (representing equilibration in mantle) are plotted for comparison. These plots indicate that spinel from Isua and Pilbara samples are similar to those of cumulates, but are different from those of mantle peridotites. Data sources: compiled spinel from Isua ultramafic rocks: Szilas et al. (2015); the spinel field of cumulates is fit by spinel data from the Uralian-Alaskan type intrusions (Abdallah et al., 2019; Garuti et al., 2003; Himmelberg and Loney, 1995; Krause et al., 2011; Thakurta et al., 2008), the Mesoarchean Seqi Ultramafic Complex of southwestern Greenland (Szilas et al., 2018) and data compiled in Barnes and Roeder (2001); the spinel field of arc peridotites is fit by spinel data in Ionov (2010), Parkinson and Pearce (1998) and Tamura and Arai (2006); the spinel field of abyssal peridotites is fitted by spinel data in Khedr et al. (2014), Standish et al.

(2002) and Tamura and Arai (2006). Spinel Fe-Tl, Cr-Al and metamorphic trends are from Barnes and Roeder (2001).

In summary, rock textures found in Isua ultramafic rocks (i.e., polygonal textures) also occur in Pilbara ultramafic samples. Pilbara ultramafic rocks potentially have similar primary mineral assemblages (olivine + spinel ± pyroxene) compared to those of the Isua ultramafic rocks, although their alteration overprints differ. Ultramafic rocks from the Isua supracrustal belt show broadly similar HSE characteristics versus the Pilbara ultramafic rocks, although peridotites from enclaves in the meta-tonalite body south of the Isua supracrustal belt exhibit lower $(Pt/Ir)_{PM}$ values. The rocks have broadly similar geochemical characteristics in other whole-rock major and trace elements and spinel geochemistry. With our sample set, it is not possible to know whether Isua and Pilbara ultramafic rocks share similar olivine microstructures or oxygen isotopic systematics.

5.3. Are plate tectonic mantle slices necessary for explaining Isua ultramafic rocks?

In this section, we expand our comparison between Isua and Pilbara ultramafic rocks to other ultramafic rocks and comparing our findings with those of similarly altered compiled and modelled cumulates and mantle peridotites to establish whether any feature of Isua ultramafic rocks needs to be explained uniquely via plate tectonic-related mantle slices. Although the polygonal textures of Isua ultramafic rocks (e.g., Nutman et al., 1996) and the B-type olivine fabrics (Kaczmarek et al., 2016) have been interpreted to reflect mantle environments, these rock textures are also consistent with cumulate origins. First, the polygonal textures need not reflect equilibration under mantle conditions (cf. Nutman et al., 1996) as these fabrics occur in Pilbara ultramafic samples and other olivine-rich cumulates as potential products of recrystallization (e.g., Hunter, 1996). Moreover, a CPO pattern of B-type olivine fabrics does not need to be produced by deformation via dislocation creep in hydrated mantle wedge environments (cf. Kaczmarek et al., 2016). Formation of B-type fabrics in primary or secondary olivine grains is possible under crustal conditions, where olivine deformation may be accomplished by a range of dislocation slip systems or other growth and/or deformation mechanisms (e.g., dissolution creep) (Chin et al., 2020; Holtzman et al., 2003; Liu et al., 2018; Nagaya et al., 2014a, 2014b; Wheeler et al., 2001; Yao et al., 2019). In particular, a B-type CPO pattern can be produced in igneous olivine grains via the formation of a shape-preferred orientation of olivine crystals with the presence of melts and a stress field (e.g., during the compaction of a cumulate mush) (e.g., Yao et al., 2019; Chin et al., 2020; Holtzman et al., 2003). Such a CPO pattern can also be found in secondary olivine grains overgrowing the strongly oriented serpentine matrix, where olivine growth is associated with prograde metamorphism not necessarily under mantle conditions (Nagaya et al., 2014a; 2014b; cf. Nozaka, 2014). Therefore, with current rock and mineral textural data from Isua ultramafic rocks, mantle wedge conditions are not required, and cumulate origins are viable.

Igneous and metamorphic conditions reflected by mineral assemblages of Isua ultramafic rocks are important for constraining their origins. Primary mineral assemblages of the Isua ultramafic rocks (i.e., olivine + spinel ± pyroxene) are consistent with both mantle and cumulate origins. Recently, Nutman et al. (2020) interpreted the metamorphic assemblages, including occurrences of Ti-humite phases to reflect low-temperature (<500 ˚C), UHP (>2.6 GPa) metamorphism, which can only occur in sub-arc mantle environments (Friend and Nutman, 2011; Nutman et al., 2020). However, there are several features in the Isua ultramafic rocks that suggest that Ti-humite could be stable at substantially lower pressures, possibly as shallow as crustal conditions consistent with regional amphibolite facies metamorphism. First, the experiment of Shen et al. (2015) have been performed with a mineral assemblage and bulk rock composition that is significantly different from those of the Isua rocks. Most importantly, these experiments did not include the effects of CO_2 or halogens. Although Ti-humite in Isua ultramafic samples have low halogen concentrations (e.g., Table S2; Guotana et al., 2021), the effect of carbonate phases cannot be ignored. In Isua sample AW17724-2C, magnesite is commonly found together with olivine and Ti-humite phases. Magnesite is likely the reaction product of the olivine breakdown reaction forming atg+mag+Fe-oxide. In the presence of Ti-phases the same olivine breakdown can be associated with the formation of Ti-humite phases and later talc (e.g., **Figs. 2a, 10d**; cf. Guotana et al., 2021). The absence of brucite indicates an active role of CO_2 in the thermodynamic relevant chemical system. Therefore, the carbonate-free experimental results from Shen et al. (2015) are not directly applicable to Isua ultramafic rocks (cf. Nutman et al., 2020). We note that the presence of carbonates or high XCO_2 conditions could significantly lower the pressure required for the formation of Ti-humite phases. For example, both Ti-clinohumite and Ti-chondrodite have been reported in marbles that experienced contact metamorphism at amphibolite facies conditions, where carbonates have been interpreted to play an essential role in reactions forming Ti-humite phases (e.g., Ehlers and Hoinkes, 1987).

The observed mineral assemblage (i.e., olivine + serpentine ± Ti-humite ± magnesite± talc) can be used to constrain the metamorphic conditions even though no reliable thermodynamic data for Ti-humite phases are available. Ignoring Ca, Al, Ti and F, i.e., in a simplified $MgO–SiO_2–H_2O–CO_2$ system, the observed reaction of forsterite + CO_2 = magnesite + talc as well as the antigorite forming reaction is limited to a temperature maximum of 630 °C at 2 GPa (**Fig. 10b**). We note that decreasing pressure increases the range of fluid composition (XCO_2) in which the reaction and thus the observed mineral assemblage can occur (**Fig. 10a-c**). Moreover, the temperature range is in strong agreement with the crustal-level metamorphic conditions determined for the supracrustal rocks of the belt (Ramirez-Salazar et al., 2021). Based on these findings, the possible formation pressures of Ti-humite phases in Isua ultramafic rocks could be far lower than previously interpreted (Nutman et al., 2020), potentially matching amphibolite facies conditions (e.g., Ehlers and Hoinkes, 1987) that are recorded across the whole Eoarchean Isua supracrustal belt (Ramírez-Salazar et al., 2021; Rollinson, 2002; Gauthiez-Putallaz et al., 2020). Interestingly, both Ti-chondrodite and Ti-clinohumite (which are also associated with magnesite + olivine + serpentine) were found in one other sample by Dymek et al. (1988a) collected from an outcrop within the Isua supracrustal belt located ~5 km south of the two meta-peridotite ultramafic lenses (**Fig. 1**) (Nutman and Friend, 2009). Based on the chondrite-normalized REE pattern of this sample and geochemical and petrological evidence from seven other samples from this outcrop (Dymek et al., 1988b), Dymek et al. (1988a) concluded that this outcrop does not represent a mantle slice. Hence, this Ti-humite bearing sample from Dymek et al. (1988a) can, in turn, potentially be evidence of crustal origins of Ti-humite phases in ultramafic rocks of the Isua supracrustal belt.

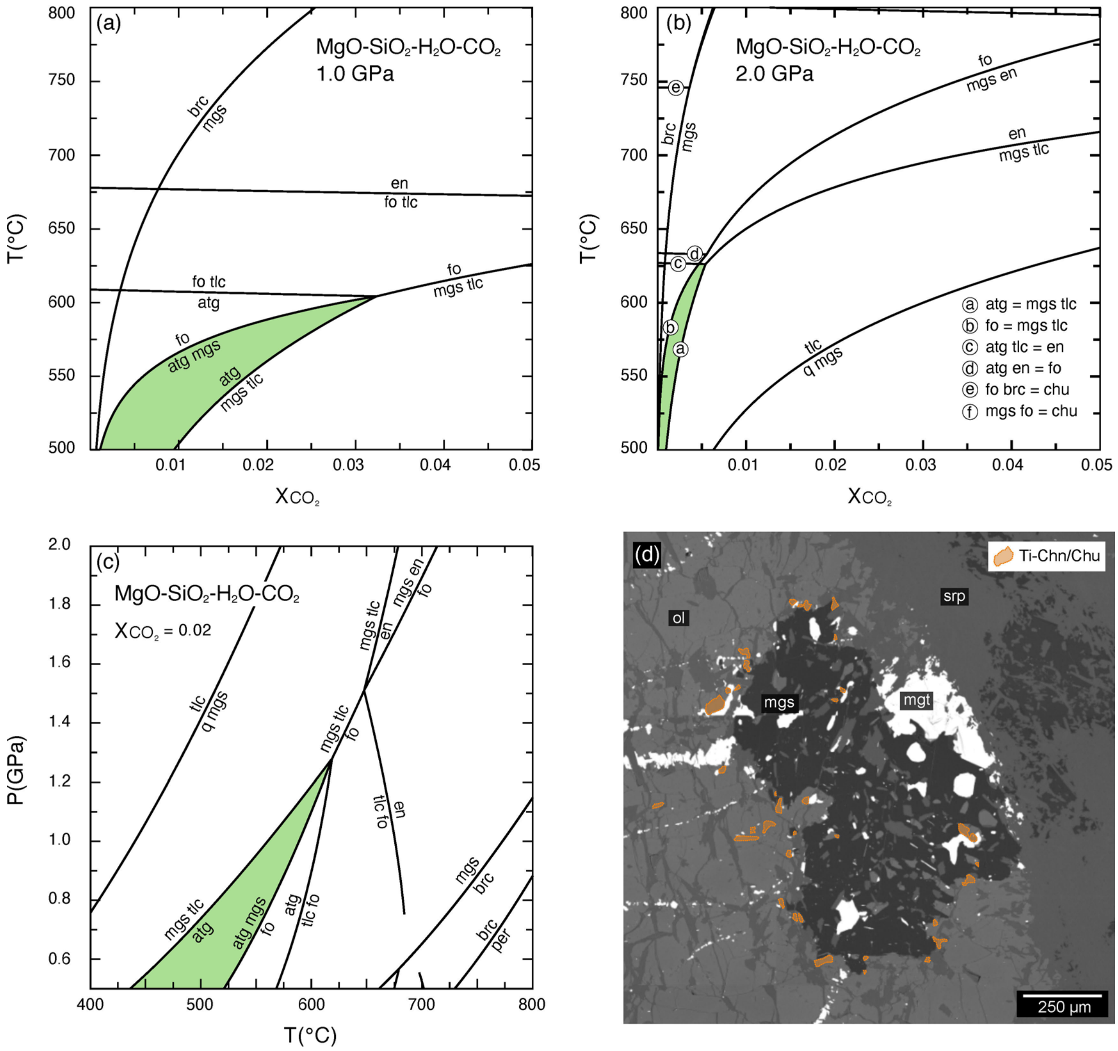

Figure 10: Schreinemarkers diagrams showing the olivine breakdown reactions forming antigorite+magnesite and the stability fields of relevant phases in temperature (T) versus X(CO_2) space at two different pressures (panels a-b) and the stability fields in T versus pressure (P) space at X(CO_2) = 0.02 (panel c). Calculations were performed with Perple_X (Connolly, 2005) (version 6.9.0) and an updated version of the internally consistent Holland and Powell (2011) dataset (ds63 update). The stability fields of Ti-humite phases cannot be calculated due to a lack of relevant thermodynamic data. Nonetheless, co-existing phases of Ti-humite (i.e., magnesite, forsteritic olivine and talc) in Isua sample AW17724-2C are consistent with metamorphism under crustal conditions and 500–650 °C in the presence of CO_2 (panel d). This is potentially consistent with the regional amphibolite metamorphism affecting the Isua supracrustal belt (Ramírez-Salazar et al., 2021). Abbreviations: atg: antigorite; brc: brucite; chu: clinohumite; en: enstatite; fo: forsterite; mgs: magnesite; q: quartz; per: periclase; tlc: talc.

Whole-rock and trace element characteristics of ultramafic rocks may help to discern crustal igneous rocks from tectonic mantle slices. This is because crustal igneous rocks should have geochemical signatures corresponding to mantle melts, their crystal precipitates assimilation effects and/or post-cumulus modifications, whereas mantle slices should show geochemical evidence reflecting melt-depletion and re-enrichment under mantle conditions. To facilitate petrogenetic interpretation for rocks with potentially complex alteration histories (see section 5.1), we compare Isua and Pilbara ultramafic rocks with (1) modelled melt-refertilized abyssal peridotites generated by combining batch melting models (calculated using pMELTS; Ghiorso et al., 2002) and mixing models (Chin et al., 2014); (2) variably altered (including melt infiltrated and fluid infiltrated) arc peridotites; (3) variably altered abyssal peridotites; (4) cumulates (which largely experienced serpentinization) from Archean terranes and Phanerzoic settings; (5) modelled cumulates of hydrous and anhydrous Phanerzoic settings (calculated using alphaMELTS; Ghiorso and Sack, 1995; Smith and Asimow, 2005) as presented in Chin et al. (2018); and (6) komatiites (see **Figs 5–9** captions for references from which the literature data were compiled).

We find that both Isua and Pilbara ultramafic rocks show similar whole-rock major element geochemistry to the compiled mantle peridotites (e.g., melt-refertilized forearc peridotites from mantle wedges and abyssal peridotites from mid-ocean ridges; **Fig. 5**) and the most Mg-rich cumulates that represent <10% fractional crystallization products of basaltic melts (**Fig. 6**). Although the Isua and Pilbara ultramafic rocks generally have systematically less CaO compared with mantle peridotites, possibly due to low to zero abundances of clinopyroxene (**Fig. 5**), this can also be explained by alteration effects (see section 5.1). In fact, small clinopyroxene inclusions occur in olivine grains of some Isua ultramafic rocks from lens A, which have been explained as indicative of olivine participation coupled with clinopyroxene dissolution during reactions between mantle peridotites and ascending melts (Nutman et al., 2021). However, we note that clinopyroxene undersaturation and olivine saturation is possible across a range of pressure-temperature-composition combinations (Chen and Zhang, 2009 and references therein) and could happen under crustal conditions during magma crystallization in the presence of water, crustal assimilation and/or magma recharge (e.g., Kelemen, 1990; Gordeychik et al., 2018). Because Al_2O_3 is unlikely to be significantly mobilized during fluid-assisted alterations (see section 5.1), the negatively correlated MgO and Al_2O_3 found in these Isua and Pilbara ultramafic samples should reflect primary igneous features or melt-assisted interactions (note that MgO concentrations for most samples may not be significantly altered, **Fig. 4b**). We therefore interpret that the observed major element geochemical systematics reflect either (1) depleted mantle peridotites that were variably altered by percolating melts (e.g., Friend and Nutman, 2011; Nutman et al., 2021; Van de Löcht et al., 2020) or (2) Mg-rich cumulates that were variably contaminated by co-existing, more evolved melts (e.g., Szilas et al., 2015).

Compared to Isua and Pilbara ultramafic samples, most depleted mantle rocks from plate tectonic settings generally show much stronger depletions in many trace elements versus primitive mantle values (**Fig. 7**), as highlighted by their $(La/Sm)_{PM}$, $(Gd/Yb)_{PM}$, and Th values, possibly because of strong melt depletion as expected for tectonically-emplaced mantle residues. Elevation of trace element concentrations is expected during some alterations (see section 5.1), but fluid-assisted alterations (including serpentinization and talc carbonate alteration) alone cannot produce the observed trace element geochemistry of Isua and Pilbara ultramafic samples (**Fig. 8a–b**). Instead, some mantle rocks (modified by melt-rock interactions), and also cumulate rocks, have comparable trace element geochemistry (**Fig. 7**). Indeed, similarities between trace element patterns of Isua ultramafic rocks and those of nearby basalts (Friend and Nutman, 2011; Szilas et al., 2015; Van de Löcht et al., 2020) were explained by (1) reactions between mantle resitites and melts (Friend and Nutman, 2011; Nutman et al., 2021; Van de Löcht et al., 2020) or (2) reactions between melt components (e.g., evolving basaltic melts) and cumulus minerals (Szilas et al., 2015). Therefore, the observed generally flat, primitive-mantle-like trace element characteristics found in new and compiled Isua and Pilbara samples are consistent with both depleted mantle residue or cumulate origins.

Relatively high primitive mantle-normalized Os, Ir, and Ru versus Pt, Pd and Re [e.g., $(Pt/Ir)_{PM} < 1$] is often used to discriminate depleted mantle rocks because Pt, Pd and Re behave as moderately incompatible elements during mantle melting (e.g., Bockrath et al., 2004; Wang et al., 2013). However, we note that during mantle melting, I-PGEs typically show similar compatibility [such that $(Ru/Ir)_{PM} \approx 1$], whereas in the studied Pilbara samples, significant fractionation among I-PGEs [i.e., >2 $(Ru/Ir)_{PM}$ values] are observed (**Fig. 8**). Although mantle rocks which suffered extensive melt-rock interactions could also have strongly fractionated HSEs (e.g., Büchl et al., 2002; Ackerman et al., 2009), their overall HSE trends [including $(Pt/Ir)_{PM}$ and $(Ru/Ir)_{PM}$ values] are dissimilar to those of Pilbara samples (**Fig. 8b**). In contrast, some chromite-bearing peridotite cumulates from layered intrusions show similar HSE fractionation trends versus Pilbara samples (**Fig. 8c**). Therefore, HSE patterns of the Pilbara samples are consistent with the proposed cumulate origin of these rocks depicted from their rock textures (see above, **Fig. 3**) and spinel geochemistry (see below, **Fig. 9**). The elevated Pd and/or Re as well as unrealistic Re-Os systematics in some Pilbara samples may result from an addition of Fe-sulphides during later alteration events (see section 5; Lorand and Luguet, 2016). These Fe-sulphides then would have been altered to magnetite (which commonly occurs in alteration veins or triple junction points of serpentine clusters of Pilbara samples, **Fig. 3b**) over billions of years. In comparison, ultramafic rocks from the Isua supracrustal belt (including dunites from the lenses; **Fig. 8a**; Szilas et al., 2015) and meta-tonalite enclaves south of the Isua supracrustal belt (**Fig. 8a**, Van de Löcht et al., 2018) show a range of HSE patterns, highlighted by their <0.5 to >10 $(Ru/Ir)_{PM}$ and $(Pt/Ir)_{PM}$ values. Significantly elevated $(Ru/Ir)_{PM}$ and $(Pt/Ir)_{PM}$ values may be explained by interactions with melts; such interactions could happen to both cumulates and mantle peridotites (e.g., Ackerman et al., 2009; Gannoun et al., 2016; Szilas et al., 2015). Although some Isua ultramafic rocks have $(Ru/Ir)_{PM}$ close to 1 and $(Pt/Ir)_{PM}$ less than 1 [e.g., "group 1" peridotites sampled from meta-tonalite enclaves (Van de Löcht et al., 2018) and a portion of ultramafic rocks studied by Szilas et al. (2015)], which are similar to depleted abyssal mantle rocks (Wang et al., 2013), such patterns also occur in cumulates (**Fig. 8c**) (McIntyre et al., 2019; Szilas et al., 2014; 2018). McIntyre et al. (2019) argue that these specific HSE patterns may be alternatively explained by preferential partitioning of I-PGEs into cumulus phases such as olivine and chromite. Therefore, HSEs may not be as discriminative as previously thought in terms of recognizing depleted mantle rocks. Accordingly, HSE patterns of Pilbara and Isua ultramafic rocks, including those from meta-tonalite enclaves south of the Isua supracrustal belt, can be explained by cumulate origins (± modifications potentially by melts).

Some spinel crystals with ~100 Cr# and ~0 Mg# values in the new and compiled Isua ultramafic rocks reflect metamorphic modifications of primary chromite into magnetite (**Fig. 3b**; Barnes and Roeder, 2001). However, igneous petrogenesis can be interpreted from primary chromite grains of both Isua and Pilbara ultramafic samples. New and compiled spinel data [from Szilas et al. (2015) which were obtained from rocks of lenses A and B] of these rocks match the Fe–Ti trend in the Mg#–Cr# space (**Fig. 9b**). Such a trend can be produced by equilibration of spinel phases during fractional crystallization (Barnes and Roeder, 2001), and thus can be found in cumulates (**Fig. 9b**). In contrast, due to equilibration with olivine, mantle spinel typically has high Mg# and varied Cr# (i.e., the Cr–Al trend in **Fig. 9b**, Barnes and Roeder, 2001) as well as low TiO_2 (**Fig. 9a**) (e.g., Tamura and Arai, 2006). Although fluid/melt assisted alterations could impact spinel geochemistry in mantle rocks, expected changes include Cr# reduction and Mg# increase along the Cr–Al trend (El Dien et al., 2019), which are not consistent with the observed spinel geochemistry. Therefore, we conclude that some chromite spinel crystals from Isua (Szilas et al., 2015) and Pilbara ultramafic rocks are not similar to spinel hosted in mantle rocks, but rather indicate cumulate origins (cf. Nutman et al., 2021).

Olivine oxygen isotopes of some dunites from the Isua supracrustal rocks are interpreted to be mantle-like and indicative of fluid metasomatism (likely from recycling hydrated crust) in the mantle wedge (Nutman et al., 2021). This material exchange between surface and mantle is thought to be exclusive to plate tectonic subduction settings (Nutman et al., 2020; Nutman et al., 2021). However, such material exchange is also possible for hot stagnant-lid settings, accomplished by recycling of the buried or dripping hydrated crustal materials (see tectonic models introduced in section 2; also, Moore and Webb, 2013; Smithies et al., 2007). Indeed, mantle-like oxygen isotopes are observed in zircons from some tonalites (originally lower crust partial melts) of the East Pilbara Terrane (where its geometry and structures largely suggest non-plate tectonic origins, see section 2.2; Smithies et al., 2021). This finding implies a fluid-rich early mantle, buffered by fluxing from the recycled crust, that was capable of introducing mantle-like oxygen isotope signatures to early crust and magmas (Smithies et al., 2021). Therefore, mantle-like oxygen isotopic signatures found in some dunites from the Isua supracrustal belt need not be explained by plate tectonic subduction (cf. Nutman et al., 2021).

In summary, although several features of Isua or Pilbara ultramafic samples are commonly associated with depleted mantle rocks (e.g., the B-type olivine fabrics and Ti-humite preserved in Isua ultramafic samples), these features are not inconsistent with cumulate origins. In addition, the cumulate textures of Pilbara ultramafic samples and the spinel geochemical characteristics of both Isua and Pilbara ultramafic samples are inconsistent with tectonically-emplaced depleted mantle, but instead are compatible with cumulate origins (**Figs. 4–9**). As such, both Isua and Pilbara ultramafic samples can be interpreted as crustal cumulates. Because crustal cumulates are produced by fractional crystallization of melts, these rocks are consistent with both plate tectonics and hot stagnant-lid tectonics. Thus, plate tectonics is not required to explain the petrogenesis of Isua ultramafic rocks (cf. Nutman et al., 2020; Nutman et al., 2021).

5.4. A model for emplacement, metamorphism and alteration of Eo- and Paleo-Archean phaneritic ultramafic rocks

As both Isua and Pilbara ultramafic rocks can be interpreted by a hot stagnant-lid tectonic regime such as heat-pipe tectonics (Moore and Webb, 2013) and partial convective overturn tectonics (Collins et al., 1998), we propose a common evolutionary pathway for ultramafic rocks of early Earth terranes. Ultramafic rocks of early Earth could have initially crystallized from high-magnesium, fluid-rich magmas, either as ultramafic volcanic flows [e.g., komatiites, Byerly et al. (2019)], intrusions, or crustal cumulates at the bases of lava flows or magma chambers (**Fig. 11**). Later, these ultramafic rocks could have been metamorphosed under crustal conditions (e.g., greenschist or amphibolite facies conditions) that may or may not have been associated with significant deformation. In the case of the Isua supracrustal belt, amphibolite facies metamorphism was accompanied by deformation during, at the end of, or after heat-pipe cooling (e.g., Ramírez-Salazar et al., 2021; Webb et al., 2020; Zuo et al., 2021). These P-T conditions are capable of producing olivine + serpentine Ti-humite + carbonate + talc bearing assemblages over the ultramafic protoliths (**Fig. 11a**). Primary igneous textures in olivine-rich cumulates could have been preserved by concentrating most of the strain into other phases (e.g., Yao et al., 2019; Zuo et al., 2021). Alternatively, growth of metamorphic olivine from dehydration breakdown of strongly oriented serpentine minerals could also produce a B-type olivine CPO (e.g., Nagaya et al., 2014a, 2014b; cf. Nozaka, 2014). In comparison, hot stagnant-lid volcanism during the Paleoarchean time would have been less rapid in terms of long-term deposition and burial rates versus the Eoarchean Isua supracrustal belt, and thus would have led to a relatively hot lithosphere for the East Pilbara Terrane (Moore and Webb, 2013; Webb et al., 2020), potentially permitting intra-crustal partial convection via gravitational instability (**Fig. 11b**; Collins et al., 1998). The metamorphic conditions experienced by the exposed Pilbara rocks may have been lower, and deformation may have been weaker (e.g., Collins et al., 1998; Wiemer et al., 2018), especially in rocks located far from the margins of the granitoid bodies (e.g., François et al., 2014) such as the samples studied here (**Fig. 1b**). Consequently, Pilbara ultramafic samples only preserve evidence for greenschist metamorphism without identifiable strain (**Fig. 3**). Post-deformational alterations (such as talc, carbonate, or serpentine alterations) might have further modified these ultramafic rocks as well as nearby supracrustal rocks in the following >3 billion years (**Fig. 11**).

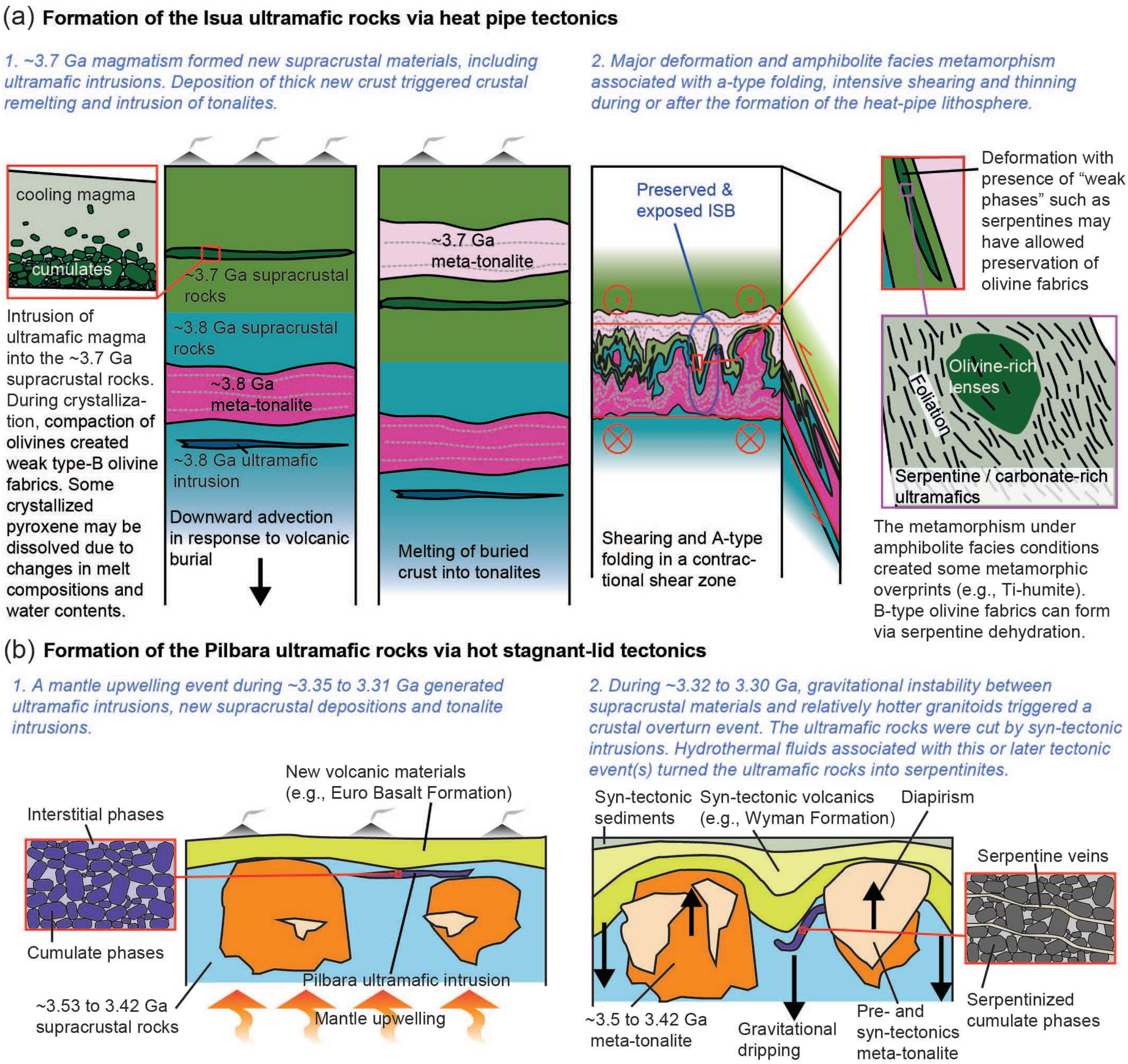

Figure 11. Evolutionary diagrams for Isua and Pilbara ultramafic rocks. Ultramafic rocks from both terranes can be interpreted via similar hot stagnant-lid tectonic models. Ultramafic rocks are initially cumulates formed during cooling of magmas in hot stagnant-lid settings that feature voluminous volcanism. These cumulates were then variably deformed and/or metamorphosed during tectonic events that either represent (1) shortening, corresponding to volcanic burial, plate-breaking or plate tectonic subduction (panel **a**); or (2) intra-crustal diapirism corresponding to gravitational instability (panel **b**). Later, mostly static (talc/carbonate/serpentine) alterations further modified the petrology and geochemistry.

6. Conclusions

Some ultramafic rocks preserved in or near the Isua supracrustal belt have been interpreted as tectonically emplaced mantle peridotites that require >3.7 Ga onset of plate tectonics (e.g., Nutman et al., 2020; Van de Löcht et al., 2018). In contrast, this study shows that: (1) the polygonal rock textures of Isua ultramafic samples can also be observed in Pilbara ultramafic rocks which show rock textures of crustal cumulates; (2) the whole-rock major element, trace element and HSE patterns of Isua ultramafic rocks are similar to those of Pilbara ultramafic rocks and/or crustal cumulates; (3) the co-existence of Ti-humite, magnesite, serpentine, olivine, clinopyroxene and perhaps talc may be compatible with crustal conditions; (4) the olivine oxygen isotopic signatures of Isua ultramafic rocks can be explained by mantle-derived or metamorphic fluid fluxing in a hot stagnant-lid setting or a plate tectonic subduction setting; (5) the CPO inferred B-type olivine fabrics are consistent with crustal cumulates; and (6) the spinel geochemistry of Isua ultramafic rocks is only compatible with crustal cumulates. In summary, many petrological and geochemical aspects (e.g., rock and mineral textures, Ti-humite phases, and normalized HSE patterns) of phaneritic ultramafic rocks in early Earth terranes on Earth could be explained in the contexts of tectonically-emplaced mantle slices atop of crustal rocks, but are also consistent with crustal cumulates (cf. Nutman et al., 2021). In contrast, other characteristics of these rocks, such as certain types of spinel geochemistry (e.g., Fe-Ti trends in Cr#-Mg# space, Barnes and Roeder, 2001) as well as cumulate textures, appear to be unique to cumulates. Thus, we conclude that no features preserved in ultramafic rocks of the Isua supracrustal belt and East Pilbara Terrane are diagnostic of plate tectonic-related mantle slices, but instead are compatible with crustal cumulates. We argue that differences between ultramafic rocks within two terranes only reflect contrasting metamorphism, deformation, and/or alteration conditions experienced by these rocks, not necessarily different protoliths (cf. Friend and Nutman, 2011; Nutman et al., 2020). Again, it is important to note that these interpretations do not exclude plate tectonic origins for the formation of the Isua supracrustal belt (e.g., Van Kranendonk, 2010; Nutman et al., 2020), but they permit a hot stagnant-lid tectonic origin for this terrane, consistent with previous studies for the belt (Ramírez-Salazar et al., 2021; Webb et al., 2020; Zuo et al., 2021). Therefore, because the East Pilbara Terrane (e.g., Collins et al., 1998; Van Kranendonk et al., 2007) can also be explained in terms of a hot stagnant-lid setting, no tectonic shift between the Eoarchean and Paleoarchean is required. Short episodes of local plate tectonic processes during the Eo- and Paleoarchean might be possible, as regional stagnant-lid processes may have coexisted with local plate tectonic processes in early terrestrial planets (e.g., Van Kranendonk, 2010; Yin, 2012a; Yin, 2012b). Nonetheless, our findings show that a ≤3.2 Ga initiation of plate tectonics is viable.

Acknowledgements

We thank An Li for his sampling assistance, Martin Van Kranendonk for field logistics advice, and Gary Byerly for insights on igneous textures and petrogenesis. Funding support comes from the American Chemical Society Petroleum Research Fund (PRF-53549-ND8), start-up funds from the University of Hong Kong, and the General Research Fund of the Hong Kong Research Grants Council (#17305718), all to A.A.G.W. Reviewer contributions are gratefully acknowledged. L. A. acknowledges the support of the Czech Science Foundation through the project no. 19-08066S and institutional support RVO67985831 of the Institute of Geology of the Czech Academy of Sciences. Reviewer contributions are gratefully acknowledged.

Data Availability Statement

Datasets for this research are included in the Supporting Information file (Table S1 to S3), and references. Datasets generated by this research can also be found at the DataHub repository (https://datahub.hku.hk/) following the link https://doi.org/10.25442/hku.14220047.

References

Abdallah, S. E., S. Ali, and M. A. Obeid (2019), Geochemistry of an Alaskan-type mafic-ultramafic complex in Eastern Desert, Egypt: New insights and constraints on the Neoproterozoic island arc magmatism, *Geoscience Frontiers*, *10*(3), 941-955. https://doi.org/10.1016/j.gsf.2018.04.009

Ackerman, L., R. J. Walker, I. S. Puchtel, L. Pitcher, E. Jelínek, and L. Strnad (2009), Effects of melt percolation on highly siderophile elements and Os isotopes in subcontinental lithospheric mantle: a study of the upper mantle profile beneath Central Europe, *Geochimica Et Cosmochimica Acta*, *73*(8), 2400-2414. https://doi.org/10.1016/j.gca.2009.02.002

Aldanmaz, E., and N. Koprubasi (2006), Platinum-group-element systematics of peridotites from ophiolite complexes of northwest Anatolia, Turkey: implications for mantle metasomatism by melt percolation in a supra-subduction zone environment, *International Geology Review*, *48*(5), 420-442. https://doi.org/10.2747/0020-6814.48.5.420

Arai, T., S. Omori, T. Komiya, and S. Maruyama (2015), Intermediate P/T-type regional metamorphism of the Isua Supracrustal Belt, southern west Greenland: The oldest Pacific-type orogenic belt?, *Tectonophysics*, *662*, 22-39. https://doi.org/10.1016/j.tecto.2015.05.020

Barnes, S. J., and P. L. Roeder (2001), The range of spinel compositions in terrestrial mafic and ultramafic rocks, *Journal of Petrology*, *42*(12), 2279-2302. https://doi.org/10.1093/petrology/42.12.2279

Barnes, S. J., D. R. Mole, M. Le Vaillant, M. J. Campbell, M. R. Verrall, M. P. Roberts, and N. J. Evans (2016), Poikilitic textures, heteradcumulates and zoned orthopyroxenes in the Ntaka Ultramafic Complex, Tanzania: implications for crystallization mechanisms of oikocrysts, *Journal of Petrology*, *57*(6), 1171-1198. https://doi.org/10.1093/petrology/egw036

Bauer, A., J. Reimink, T. Chacko, B. Foley, S. Shirey, and D. J. G. P. L. Pearson (2020), Hafnium isotopes in zircons document the gradual onset of mobile-lid tectonics, *Geochemical Perspectives Letters*, *14*, 1-6. https://doi.org/10.7185/geochemlet.2015

Beall, A., L. Moresi, and C. M. Cooper (2018), Formation of cratonic lithosphere during the initiation of plate tectonics, *Geology*, *46*(6), 487-490. https://doi.org/10.1130/G39943.1

Bédard, J. H. (2018), Stagnant lids and mantle overturns: Implications for Archaean tectonics, magmagenesis, crustal growth, mantle evolution, and the start of plate tectonics, *Geoscience Frontiers*, *9*(1), 19-49. https://doi.org/10.1016/j.gsf.2017.01.005

Becker, H., M. Horan, R. Walker, S. Gao, J.-P. Lorand, and R. Rudnick (2006), Highly siderophile element composition of the Earth's primitive upper mantle: constraints from new data on peridotite massifs and xenoliths, *Geochimica Et Cosmochimica Acta*, *70*(17), 4528-4550. https://doi.org/10.1016/j.gca.2006.06.004

Birck, J. L., M. R. Barman, and F. Capmas (1997), Re-Os isotopic measurements at the femtomole level in natural samples, *Geostandards newsletter*, *21*(1), 19-27. https://doi.org/10.1111/j.1751-908X.1997.tb00528.x

Bland, M. T., and W. B. McKinnon (2016), Mountain building on Io driven by deep faulting, *Nature*, *9*(6), 429-432, doi:10.1038/ngeo2711. https://doi.org/10.1038/ngeo2711

Bockrath, C., C. Ballhaus, and A. Holzheid (2004), Fractionation of the platinum-group elements during mantle melting, *Science*, *305*(5692), 1951-1953. https://doi.org/10.1126/science.1100160

Boudier, F., G. Ceuleneer, and A. Nicolas (1988), Shear zones, thrusts and related magmatism in the Oman ophiolite: initiation of thrusting on an oceanic ridge, *Tectonophysics*, *151*(1-4), 275-296. https://doi.org/10.1016/0040-1951(88)90249-1

Brown, M., and T. Johnson (2018), Secular change in metamorphism and the onset of global plate tectonics, *American Mineralogist*, *103*(2), 181-196. https://doi.org/10.2138/am-2018-6166

Büchl, A., G. Brügmann, V. G. Batanova, C. Münker, and A. W. Hofmann (2002), Melt percolation monitored by Os isotopes and HSE abundances: a case study from the mantle section of the Troodos Ophiolite, *Earth and Planetary Science Letters*, *204*(3-4), 385-402. https://doi.org/10.1016/S0012-821X(02)00977-9

Byerly, G., D. Lowe, and C. Heubeck (2019), Geologic evolution of the Barberton Greenstone Belt–a unique record of crustal development, surface processes, and early life 3.55 to 3.20 Ga, *Earth's oldest rocks, 2nd edn. Elsevier, Berlin*. https://doi.org/10.1016/B978-0-444-63901-1.00024-1

Cawood, P. A., C. J. Hawkesworth, S. A. Pisarevsky, B. Dhuime, F. A. Capitanio, and O. Nebel (2018), Geological archive of the onset of plate tectonics, *J Philosophical Transactions of the Royal Society A: Mathematical, Physical Engineering Sciences*, *376*(2132), 20170405. https://doi.org/10.1098/rsta.2017.0405

Chen, Y., and Y. Zhang (2009), Clinopyroxene dissolution in basaltic melt, *Geochimica Et Cosmochimica Acta*, *73*(19), 5730-5747. https://doi.org/10.1016/j.gca.2009.06.016

Chen, B.-Y., J.-J. Yu, and S.-J. Liu (2018), Source characteristics and tectonic setting of mafic–ultramafic intrusions in North Xinjiang, NW China: insights from the petrology and geochemistry of the Lubei mafic–ultramafic intrusion, *Lithos*, *308*, 329-345. https://doi.org/10.1016/j.lithos.2018.03.016

Chin, E. J., C.-T. A. Lee, and J. D. Barnes (2014), Thickening, refertilization, and the deep lithosphere filter in continental arcs: Constraints from major and trace elements and oxygen isotopes, *Earth and Planetary Science Letters, 397*, 184-200. https://doi.org/10.1016/j.epsl.2014.04.022

Chin, E. J., K. Shimizu, G. M. Bybee, and M. E. Erdman (2018), On the development of the calc-alkaline and tholeiitic magma series: A deep crustal cumulate perspective, *Earth and Planetary Science Letters*, *482*, 277-287. https://doi.org/10.1016/j.epsl.2017.11.016

Chin, E. J., V. Soustelle, and Y. Liu (2020), An SPO-induced CPO in composite mantle xenoliths correlated with increasing melt-rock interaction, *Geochimica Et Cosmochimica Acta*, *278*, 199-218. https://doi.org/10.1016/j.gca.2019.10.002

Coggon, J. A., A. Luguet, R. O. Fonseca, J.-P. Lorand, A. Heuser, and P. W. Appel (2015), Understanding Re–Os systematics and model ages in metamorphosed Archean ultramafic rocks: a single mineral to whole-rock investigation, *Geochimica Et Cosmochimica Acta*, *167*, 205-240. https://doi.org/10.1016/j.gca.2015.07.025

Cohen, A. S., and F. G. Waters (1996), Separation of osmium from geological materials by solvent extraction for analysis by thermal ionisation mass spectrometry, *Analytica Chimica Acta*, *332*(2-3), 269-275. https://doi.org/10.1016/0003-2670(96)00226-7

Collins, W. J., M. J. Van Kranendonk, and C. Teyssier (1998), Partial convective overturn of Archaean crust in the east Pilbara Craton, Western Australia: driving mechanisms and tectonic implications, *Journal of Structural Geology*, *20*(9-10), 1405-1424. https://doi.org/10.1016/S0191-8141(98)00073-X

Condie, K. C., and S. J. Puetz (2019), Time series analysis of mantle cycles Part II: The geologic record in zircons, large igneous provinces and mantle lithosphere, *Geoscience Frontiers*, *10*(4), 1327-1336. https://doi.org/10.1016/j.gsf.2019.03.005

Connolly, J. A. D. (2005). Computation of phase equilibria by linear programming: A tool for geodynamic modeling and its application to subduction zone decarbonation. *Earth and planetary Science Letters*, 236(1-2), 524–541. doi: 10.1016/j.epsl.2005.04.033

Creaser, R., D. Papanastassiou, and G. Wasserburg (1991), Negative thermal ion mass spectrometry of osmium, rhenium and iridium, *Geochimica Et Cosmochimica Acta*, *55*(1), 397-401. https://doi.org/10.1016/0016-7037(91)90427-7

Crowley, J., J. Myers, and G. Dunning (2002), Timing and nature of multiple 3700–3600 Ma tectonic events in intrusive rocks north of the Isua greenstone belt, southern West Greenland, Geological Society of America Bulletin, 114(10), 1311-1325. https://doi.org/10.1130/0016-7606(2002)114<1311:TANOMM>2.0.CO;2

Crowley, J. (2003), U–Pb geochronology of 3810–3630 Ma granitoid rocks south of the Isua greenstone belt, southern West Greenland, Precambrian Research, 126(3-4), 235-257. https://doi.org/10.1016/S0301-9268(03)00097-4

Dymek, R. F., J. L. Boak, and S. C. Brothers (1988a), Titanian chondrodite-and titanian clinohumite-bearing metadunite from the 3800 Ma Isua supracrustal belt, West Greenland; chemistry, petrology and origin, *American Mineralogist*, *73*(5-6), 547-558. https://doi.org/10.1093/petrology/29.6.1353

Dymek, R. F., S. C. Brothers, and C. M. Schiffries (1988b), Petrogenesis of Ultramafic Metamorphic Rocks from the 3800-Ma Isua Supracrustal Belt, West Greenland, *Journal of Petrology*, *29*(6), 1353-1397, doi:DOI 10.1093/petrology/29.6.1353. https://doi.org/10.1093/petrology/29.6.1353

Ehlers, K., and G. Hoinkes (1987), Titanian chondrodite and clinohumite in marbles from the Ötztal crystalline basement, *Mineralogy and Petrology*, *36*(1), 13-25. https://doi.org/10.1007/BF01164366

El Dien, H. G., S. Arai, L.-S. Doucet, Z.-X. Li, Y. Kil, D. Fougerouse, S. M. Reddy, D. W. Saxey, and M. Hamdy (2019), Cr-spinel records metasomatism not petrogenesis of mantle rocks, *Nature Communications*, *10*(1), 1-12. https://doi.org/10.1038/s41467-019-13117-1

Elthon, D. (1992), Chemical trends in abyssal peridotites: refertilization of depleted suboceanic mantle, *Journal of Geophysical Research: Solid Earth*, *97*(B6), 9015-9025. https://doi.org/10.1029/92JB00723

Foley, B. J., D. Bercovici, and L. T. Elkins-Tanton (2014), Initiation of plate tectonics from post-magma ocean thermochemical convection, *Journal of Geophysical Research: Solid Earth*, *119*(11), 8538-8561, doi:10.1002/2014JB011121. https://doi.org/10.1002/2014JB011121

François, C., P. Philippot, P. Rey, and D. Rubatto (2014), Burial and exhumation during Archean sagduction in the East Pilbara granite-greenstone terrane, *Earth and Planetary Science Letters*, *396*, 235-251. https://doi.org/10.1016/j.epsl.2014.04.025

Friend, C. R. L., V. C. Bennett, and A. P. Nutman (2002), Abyssal peridotites > 3,800 Ma from southern West Greenland: field relationships, petrography, geochronology, whole-rock and mineral chemistry of dunite and harzburgite inclusions in the Itsaq Gneiss Complex, *Contributions to Mineralogy and Petrology*, *143*(1), 71-92, doi:10.1007/s00410-001-0332-7. https://doi.org/10.1007/s00410-001-0332-7

Friend, C. R. L., and A. P. Nutman (2011), Dunites from Isua, Greenland: A ca. 3720 Ma window into subcrustal metasomatism of depleted mantle, *Geology*, *39*(7), 663-666, doi:10.1130/G31904.1. https://doi.org/10.1130/G31904.1

Gale, A., C. A. Dalton, C. H. Langmuir, Y. J. Su, and J. G. Schilling (2013), The mean composition of ocean ridge basalts, *Geochemistry Geophysics Geosystems*, *14*(3), 489-518, doi:10.1029/2012gc004334. https://doi.org/10.1029/2012GC004334

Gannoun, A., K. W. Burton, J. M. Day, J. Harvey, P. Schiano, and I. Parkinson (2016), Highly siderophile element and Os isotope systematics of volcanic rocks at divergent and convergent plate boundaries and in intraplate settings, *Reviews in Mineralogy and Geochemistry*, *81*(1), 651-724. https://doi.org/10.2138/rmg.2016.81.11

Garuti, G., E. V. Pushkarev, F. Zaccarini, R. Cabella, and E. Anikina (2003), Chromite composition and platinum-group mineral assemblage in the Uktus Uralian-Alaskan-type complex (Central Urals, Russia), *Mineralium Deposita*, *38*(3), 312-326. https://doi.org/10.1007/s00126-003-0348-1

Gauthiez-Putallaz, L., A. Nutman, V. Bennett, and D. Rubatto (2020), Origins of high δ18O in 3.7–3.6 Ga crust: A zircon and garnet record in Isua clastic metasedimentary rocks, *Chemical Geology*, *537*, 119474. https://doi.org/10.1016/j.chemgeo.2020.119474

Geological Survey of Western Australia 2013 database, (2013). 1:100 000 GIS Pilbara 2013 update / Geological Survey of Western Australia, in: Western Australia. Department of, M., Petroleum, Exploration Incentive, S. (Eds.). Geological Survey of Western Australia, East Perth, Western Australia ©2013.

Ghiorso, M. S., and R. O. Sack (1995), Chemical mass transfer in magmatic processes IV. A revised and internally consistent thermodynamic model for the interpolation and extrapolation of liquid-solid equilibria in magmatic systems at elevated temperatures and pressures, *Contributions to Mineralogy and Petrology*, *119*(2), 197-212. https://doi.org/10.1007/s004100050036

Ghiorso, M. S., M. M. Hirschmann, P. W. Reiners, and V. C. Kress (2002), The pMELTS: A revision of MELTS for improved calculation of phase relations and major element partitioning related to partial melting of the mantle to 3 GPa, *Geochemistry, Geophysics, Geosystems*, *3*(5), 1-35. https://doi.org/10.1029/2001GC000217

Gordeychik, B., T. Churikova, A. Kronz, C. Sundermeyer, A. Simakin, and G. Wörner (2018), Growth of, and diffusion in, olivine in ultra-fast ascending basalt magmas from Shiveluch volcano, *Scientific reports*, *8*(1), 1-15. https://doi.org/10.1038/s41598-018-30133-1

Goodrich, C. A., A. M. Fioretti, M. Tribaudino, and G. Molin (2001), Primary trapped melt inclusions in olivine in the olivine-augite-orthopyroxene ureilite Hughes 009, *Geochimica Et Cosmochimica Acta*, *65*(4), 621-652. https://doi.org/10.1016/S0016-7037(00)00521-4

Guotana, J. M., T. Morishita, I. Nishio, A. Tamura, T. Mizukami, K. Tani, Y. Harigane, K. Szilas, and D. G. Pearson (2021), Deserpentinization and high-pressure (eclogite-facies) metamorphic features in the Eoarchean ultramafic body from Isua, Greenland, Geoscience Frontiers, 101298.

Hanghøj, K., P. B. Kelemen, D. Hassler, and M. Godard (2010), Composition and Genesis of Depleted Mantle Peridotites from the Wadi Tayin Massif, Oman Ophiolite; Major and Trace Element Geochemistry, and Os Isotope and PGE Systematics, *Journal of Petrology*, *51*(1-2), 201-227. https://doi.org/10.1093/petrology/egp077

Hansen, V. (2007), Subduction origin on early Earth: A hypothesis, *Geology*, *35*(12), 1059-1062. https://doi.org/10.1130/G24202A.1

Harrison, T. M. (2009), The Hadean Crust: Evidence from > 4 Ga Zircons, *Annual Review of Earth and Planetary Sciences*, *37*, 479-505. https://doi.org/10.1146/annurev.earth.031208.100151

Hickman, A. H. (2021), EAST PILBARA CRATON: A RECORD OF ONE BILLION YEARS IN THE GROWTH OF ARCHEAN CONTINENTAL CRUST, *Geological Survey of Western Australia, Report 143*, 1-187.

Himmelberg, G. R., and R. A. Loney (1995), *Characteristics and petrogenesis of Alaskan-type ultramafic-mafic intrusions, southeastern Alaska*, US Government Printing Office. https://doi.org/10.3133/pp1564

Holland, T. J. B., and R. Powell (2011), An improved and extended internally consistent thermodynamic dataset for phases of petrological interest, involving a new equation of state for solids, *Journal of Metamorphic Geology*, *29*(3), 333-383. https://doi.org/10.1111/j.1525-314.2010.00923.x

Holtzman, B. K., D. L. Kohlstedt, M. E. Zimmerman, F. Heidelbach, T. Hiraga, and J. Hustoft (2003), Melt segregation and strain partitioning: Implications for seismic anisotropy and mantle flow, *Science*, *301*(5637), 1227-1230. https://doi.org/10.1126/science.1087132

Hopkins, M., T. M. Harrison, and C. E. Manning (2008), Low heat flow inferred from> 4 Gyr zircons suggests Hadean plate boundary interactions, *Nature*, *456*(7221), 493-496. https://doi.org/10.1038/nature07465

Hunter, R. (1996), Texture development in cumulate rocks, in *Developments in Petrology*, edited, pp. 77-101, Elsevier. https://doi.org/10.1016/S0167-2894(96)80005-4

Ionov, D. A. (2010), Petrology of mantle wedge lithosphere: new data on supra-subduction zone peridotite xenoliths from the andesitic Avacha volcano, Kamchatka, *Journal of Petrology*, *51*(1-2), 327-361. https://doi.org/10.1093/petrology/egp090

Janoušek, V., C. M. Farrow, and V. Erban (2006), Interpretation of whole-rock geochemical data in igneous geochemistry: Introducing Geochemical Data Toolkit (GCDkit), *Journal of Petrology*, *47*(6), 1255-1259. https://doi.org/10.1093/petrology/egl013

Johannsen, A. (1931), *A Descriptive Petrography of the Igneous Rocks: Introduction, textures, classifications and glossary*, University of Chicago Press.

Johnson, D., P. Hooper, and R. Conrey (1999), XRF Method XRF Analysis of Rocks and Minerals for Major and Trace Elements on a Single Low Dilution Li-Tetraborate Fused Bead, *Adv. X-ray anal*, *41*, 843-867.

Johnson, T. E., M. Brown, B. J. P. Kaus, and J. A. VanTongeren (2014), Delamination and recycling of Archaean crust caused by gravitational instabilities, Nature Geoscience, 7(1), 47-52, doi:10.1038/Ngeo2019. https://doi.org/10.1038/ngeo2019

Johnson, T. E., M. Brown, N. J. Gardiner, C. L. Kirkland, and R. H. Smithies (2017), Earth's first stable continents did not form by subduction, *Nature*, *543*(7644), 239-+. https://doi.org/10.1038/nature21383

Kaczmarek, M. A., S. M. Reddy, A. P. Nutman, C. R. L. Friend, and V. C. Bennett (2016), Earth's oldest mantle fabrics indicate Eoarchaean subduction, *Nature Communications*, *7*. https://doi.org/10.1038/ncomms10665

Kelemen, P. B. (1990), Reaction between ultramafic rock and fractionating basaltic magma I. Phase relations, the origin of calc-alkaline magma series, and the formation of discordant dunite, *Journal of Petrology*, *31*(1), 51-98. https://doi.org/10.1093/petrology/31.1.51

Kelemen, P. B., H. J. Dick, and J. E. Quick (1992), Formation of harzburgite by pervasive melt/rock reaction in the upper mantle, *Nature, 358(6388)*, 635-641. https://doi.org/10.1038/358635a0

Khatun, S., S. K. Mondal, M.-F. Zhou, V. Balaram, and H. M. Prichard (2014), Platinum-group element (PGE) geochemistry of Mesoarchean ultramafic–mafic cumulate rocks and chromitites from the Nuasahi Massif, Singhbhum Craton (India), *Lithos*, *205*, 322-340. https://doi.org/10.1016/j.lithos.2014.07.013

Khedr, M. Z., S. Arai, M. Python, and A. Tamura (2014), Chemical variations of abyssal peridotites in the central Oman ophiolite: evidence of oceanic mantle heterogeneity, *Gondwana Research*, *25*(3), 1242-1262. https://doi.org/10.1016/j.gr.2013.05.010

Kirkland, C., M. Hartnady, M. Barham, H. Olierook, A. Steenfelt, and J. Hollis (2021), Widespread reworking of Hadean-to-Eoarchean continents during Earth's thermal peak, *Nature Communications*, *12*(1), 1-9. https://doi.org/10.1038/s41467-020-20514-4

Knaack, C., S. Cornelius, and P. Hooper (1994), Trace element analyses of rocks and minerals by ICP-MS, *Geoanalytical Laboratory. Wash. State Univ*, *2*, 18.

Komiya, T., S. Maruyama, T. Masuda, S. Nohda, M. Hayashi, and K. Okamoto (1999), Plate tectonics at 3.8-3.7 Ga: Field evidence from the Isua Accretionary Complex, southern West Greenland, *Journal of Geology*, *107*(5), 515-554. https://doi.org/10.1086/314371

Korenaga, J. (2011), Thermal evolution with a hydrating mantle and the initiation of plate tectonics in the early Earth, *Journal of Geophysical Research: Solid Earth*, *116*(B12). https://doi.org/10.1029/2011JB008410

Krause, J., G. Brügmann, and E. Pushkarev (2011), Chemical composition of spinel from Uralian-Alaskan-type Mafic–Ultramafic complexes and its petrogenetic significance, *Contributions to Mineralogy and Petrology 161*(2), 255-273. https://doi.org/10.1007/s00410-010-0530-2

Lenardic, A. (2018), The diversity of tectonic modes and thoughts about transitions between them, *Philosophical Transactions of the Royal Society A: Mathematical, Physical and Engineering Sciences*, *376*(2132), 20170416. https://doi.org/10.1098/rsta.2017.0416

Liu, W., J. Zhang, and F. Barou (2018), B-type olivine fabric induced by low temperature dissolution creep during serpentinization and deformation in mantle wedge, *Tectonophysics*, *722*, 1-10. https://doi.org/10.1016/j.tecto.2017.10.025

Lorand, J.-P., and A. Luguet (2016), Chalcophile and siderophile elements in mantle rocks: Trace elements controlled by trace minerals, *Reviews in Mineralogy and Geochemistry*, *81*(1), 441-488. https://doi.org/10.2138/rmg.2016.81.08

Lundeen, M. T. (1978), Emplacement of the Ronda peridotite, Sierra Bermeja, Spain, *Geological Society of America Bulletin*, *89*(2), 172-180. https://doi.org/10.1130/0016-7606(1978)89<172:EOTRPS>2.0.CO;2

Maier, W. D., F. Roelofse, and S.-J. Barnes (2003), The concentration of the platinum-group elements in South African komatiites: implications for mantle sources, melting regime and PGE fractionation during crystallization, *Journal of Petrology*, *44*(10), 1787-1804. https://doi.org/10.1093/petrology/egg059

Mallik, A., S. Lambart, and E. J. Chin (2020), Tracking the evolution of magmas from heterogeneous mantle sources to eruption, in *Mantle Convection and Surface Expressions*, edited, AGU Monograph Series. https://arxiv.org/abs/2001.00928

Marchesi, C., Garrido, C. J., Proenza, J. A., Hidas, K., Varas-Reus, M. I., Butjosa, L., and Lewis, J. F., 2016, Geochemical record of subduction initiation in the sub-arc mantle: Insights from the Loma Caribe peridotite (Dominican Republic): Lithos, v. 252, p. 1-15. https://doi.org/10.1016/j.lithos.2016.02.009

Marchesi, C., C. J. Garrido, J. A. Proenza, K. Hidas, M. I. Varas-Reus, L. Butjosa, and J. F. Lewis (2016), Geochemical record of subduction initiation in the sub-arc mantle: Insights from the Loma Caribe peridotite (Dominican Republic), *Lithos*, *252*, 1-15. https://doi.org/10.1038/nature13539

McDonough, W. F., and S. S. Sun (1995), The Composition of the Earth, *Chemical Geology*, *120*(3-4), 223-253, doi:Doi 10.1016/0009-2541(94)00140-4. https://doi.org/10.1016/0009-2541(94)00140-4

McIntyre, T., D. Pearson, K. Szilas, and T. Morishita (2019), Implications for the origins of Eoarchean ultramafic rocks of the North Atlantic Craton: a study of the Tussaap Ultramafic complex, Itsaq Gneiss complex, southern West Greenland, *Contributions to Mineralogy and Petrology*, *174*(12), 1-21. https://doi.org/10.1007/s00410-019-1628-9

Moore, W. B., J. I. Simon, and A. A. G. Webb (2017), Heat-pipe planets, *Earth and Planetary Science Letters*, *474*, 13-19. https://doi.org/10.1016/j.epsl.2017.06.015

Moore, W. B., and A. A. G. Webb (2013), Heat-pipe Earth, *Nature*, *501*(7468), 501-505. https://doi.org/10.1038/nature12473

Næraa, T., A. Schersten, M. T. Rosing, A. I. S. Kemp, J. E. Hoffmann, T. F. Kokfelt, and M. J. Whitehouse (2012), Hafnium isotope evidence for a transition in the dynamics of continental growth 3.2Gyr ago, *Nature*, *485*(7400), 627-+. https://doi.org/10.1038/nature11140

Nagaya, T., S. R. Wallis, H. Kobayashi, K. Michibayashi, T. Mizukami, Y. Seto, A. Miyake, and M. Matsumoto (2014), Dehydration breakdown of antigorite and the formation of B-type olivine CPO, *Earth and Planetary Science Letters*, *387*, 67-76. https://doi.org/10.1016/j.epsl.2013.11.025

Nagaya, T., S. R. Wallis, H. Kobayashi, K. Michibayashi, T. Mizukami, Y. Seto, A. Miyake, and M. Matsumoto (2014), Reply to comment by Nozaka (2014) on; Dehydration breakdown of antigorite and the formation of B-type olivine CPO, Earth and Planetary Science Letters, 408, 406-407. https://doi.org/10.1016/j.epsl.2014.10.026

Niu, Y. L. (2004), Bulk-rock major and trace element compositions of abyssal peridotites: Implications for mantle melting, melt extraction and post-melting processes beneath mid-ocean ridges, *Journal of Petrology*, *45*(12), 2423-2458. https://doi.org/10.1016/S0012-821X(96)00218-X

Nozaka, T. (2014), Comment on; Dehydration breakdown of antigorite and the formation of B-type olivine CPO; by Nagaya et al.(2014), *Earth and Planetary Science Letters*, *408*, 402-405. https://doi.org/10.1016/j.epsl.2014.10.023

Nutman, A. P., V. C. Bennett, and C. R. Friend (2013a), The emergence of the Eoarchaean proto-arc: evolution of a c. 3700 Ma convergent plate boundary at Isua, southern West Greenland, *Geological Society, London, Special Publications*, *389*, SP389. 385. https://doi.org/10.1144/SP389.5

Nutman, A. P., V. C. Bennett, C. R. Friend, and K. Yi (2020), Eoarchean contrasting ultra-high-pressure to low-pressure metamorphisms (< 250 to> 1000° C/GPa) explained by tectonic plate convergence in deep time, *Precambrian Research*, 105770. https://doi.org/10.1016/j.precamres.2020.105770

Nutman, A. P., M. R. Scicchitano, C. R. Friend, V. C. Bennett, and A. R. Chivas (2021), Isua (Greenland)~ 3700 Ma meta-serpentinite olivine Mg# and δ18O signatures show connection between the early mantle and hydrosphere: Geodynamic implications, *Precambrian Research*, 361, 106249. https://doi.org/10.1016/j.precamres.2021.106249

Nutman, A. P., V. C. Bennett, C. R. L. Friend, H. Hidaka, K. Yi, S. R. Lee, and T. Kamiichi (2013b), THE ITSAQ GNEISS COMPLEX OF GREENLAND: EPISODIC 3900 TO 3660 Ma JUVENILE CRUST FORMATION AND RECYCLING IN THE 3660 TO 3600 Ma ISUKASIAN OROGENY, *American Journal of Science*, *313*(9), 877-911. https://doi.org/10.2475/09.2013.03

Nutman, A. P., and C. R. L. Friend (2009), New 1:20,000 scale geological maps, synthesis and history of investigation of the Isua supracrustal belt and adjacent orthogneisses, southern West Greenland: A glimpse of Eoarchaean crust formation and orogeny, *Precambrian Research*, *172*(3-4), 189-211. https://doi.org/10.1016/j.precamres.2009.03.017

Nutman, A. P., V. R. McGregor, C. R. L. Friend, V. C. Bennett, and P. D. Kinny (1996), The Itsaq Gneiss Complex of southern west Greenland; The world's most extensive record of early crustal evolution (3900-3600 Ma), *Precambrian Research*, *78*(1-3), 1-39. https://doi.org/10.1016/0301-9268(95)00066-6

O'Neill, C., and V. Debaille (2014), The evolution of Hadean–Eoarchaean geodynamics, *Earth and Planetary Science Letters*, *406*, 49-58. https://doi.org/10.1016/j.epsl.2014.08.034

O'Reilly, T. C., and G. F. Davies (1981), Magma transport of heat on Io: A mechanism allowing a thick lithosphere, *Geophysical Research Letters*, *8*(4), 313-316. https://doi.org/10.1029/GL008i004p00313

Parkinson, I. J., and J. A. Pearce (1998), Peridotites from the Izu–Bonin–Mariana forearc (ODP Leg 125): evidence for mantle melting and melt–mantle interaction in a supra-subduction zone setting, *Journal of Petrology*, *39*(9), 1577-1618. https://doi.org/10.1093/petroj/39.9.1577

Paulick, H., W. Bach, M. Godard, J. C. M. De Hoog, G. Suhr, and J. Harvey (2006), Geochemistry of abyssal peridotites (Mid-Atlantic Ridge, 15 degrees 20 ' N, ODP Leg 209): Implications for fluid/rock interaction in slow spreading environments, *Chemical Geology*, *234*(3-4), 179-210 https://doi.org/10.1016/j.chemgeo.2006.04.011

Pearce, J. A., and M. K. Reagan (2019), Identification, classification, and interpretation of boninites from Anthropocene to Eoarchean using Si-Mg-Ti systematics, *Geosphere*, *15*(4), 1008-1037. https://doi.org/10.1130/GES01661.1

Polat, A., and A. W. Hofmann (2003), Alteration and geochemical patterns in the 3.7-3.8 Ga Isua greenstone belt, West Greenland, *Precambrian Research*, *126*(3-4), 197-218. https://doi.org/10.1016/S0301-9268(03)00095-0

Ramírez-Salazar, A., T. Müller, S. Piazolo, A. A. G. Webb, C. Hauzenberger, J. Zuo, P. Haproff, J. Harvey, T. K. Wong, and C. Charlton (2021), Tectonics of the Isua supracrustal belt 1: P-T-X-d constraints of a poly-metamorphic terrane, *Tectonics*, *40*(3), e2020TC006516. https://doi.org/10.1029/2020tc006516

Reimink, J. R., J. H. Davies, A. M. Bauer, and T. Chacko (2020), A comparison between zircons from the Acasta Gneiss Complex and the Jack Hills region, *Earth and Planetary Science Letters*, *531*, 115975. https://doi.org/10.1016/j.epsl.2019.115975

Rollinson, H. (2002), The metamorphic history of the Isua greenstone belt, West Greenland, *Geological Society, London, Special Publications*, *199*(1), 329-350. https://doi.org/10.1144/GSL.SP.2002.199.01.16

Shen, T., J. Hermann, L. Zhang, Z. Lü, J. A. Padrón-Navarta, B. Xia, and T. Bader (2015), UHP metamorphism documented in Ti-chondrodite-and Ti-clinohumite-bearing serpentinized ultramafic rocks from Chinese southwestern Tianshan, *Journal of Petrology*, *56*(7), 1425-1458. https://doi.org/10.1093/petrology/egv042

Shirey, S. B., and R. J. Walker (1995), Carius tube digestion for low-blank rhenium-osmium analysis, *Analytical Chemistry*, *67*(13), 2136-2141. https://doi.org/10.1021/ac00109a036

Shirey, S. B., and R. J. Walker (1998), The Re-Os isotope system in cosmochemistry and high-temperature geochemistry, *Annual Review of Earth and Planetary Sciences*, *26*(1), 423-500. https://doi.org/10.1146/annurev.earth.26.1.423

Smith, P. M., and P. D. Asimow (2005), Adiabat_1ph: A new public front-end to the MELTS, pMELTS, and pHMELTS models, *Geochemistry, Geophysics, Geosystems*, *6*(2). https://doi.org/10.1029/2004GC000816

Smithies, R., D. Champion, M. Van Kranendonk, and A. Hickman (2007), Geochemistry of volcanic rocks of the northern Pilbara Craton, Western Australia, *Geological Survey of Western Australia Report*, *104*.

Smithies, R. H., Y. Lu, C. L. Kirkland, T. E. Johnson, D. R. Mole, D. C. Champion, L. Martin, H. Jeon, M. T. Wingate, and S. P. Johnson (2021), Oxygen isotopes trace the origins of Earth's earliest continental crust, *Nature*, *592*(7852), 70-75. https://doi.org/10.1038/s41586-021-03337-1

Snow, J. E., and H. J. Dick (1995), Pervasive magnesium loss by marine weathering of peridotite, *Geochimica Et Cosmochimica Acta, 59(20)*, 4219-4235. https://doi.org/10.1016/0016-7037(95)00239-V

Standish, J., S. Hart, J. Blusztajn, H. Dick, and K. Lee (2002), Abyssal peridotite osmium isotopic compositions from cr-spinel, *Geochemistry, Geophysics, Geosystems*, *3*(1), 1-24. https://doi.org/10.1029/2001GC000161

Stern, R. J. (2008), Modern-style plate tectonics began in Neoproterozoic time: An alternative interpretation of Earth's tectonic history, *When did plate tectonics begin on planet Earth*, *265*, 280. https://doi.org/10.1130/2008.2440(13)

Stern, R. J., T. Gerya, and P. J. Tackley (2017), Stagnant lid tectonics: Perspectives from silicate planets, dwarf planets, large moons, and large asteroids, *Geoscience Frontiers*, *9*(1). https://doi.org/10.1016/j.gsf.2017.06.004

Szilas, K., V. J. Van Hinsberg, R. A. Creaser, and A. F. M. Kisters (2014), The geochemical composition of serpentinites in the Mesoarchaean Tartoq Group, SW Greenland: Harzburgitic cumulates or melt-modified mantle?, *Lithos*, *198*, 103-116. https://doi.org/10.1016/j.lithos.2014.03.024

Szilas, K., P. B. Kelemen, and M. T. Rosing (2015), The petrogenesis of ultramafic rocks in the > 3.7 Ga Isua supracrustal belt, southern West Greenland: Geochemical evidence for two distinct magmatic cumulate trends, *Gondwana Research*, *28*(2), 565-580. https://doi.org/10.1016/j.gr.2014.07.010

Szilas, K., V. van Hinsberg, I. McDonald, T. Næraa, H. Rollinson, J. Adetunji, and D. Bird (2018), Highly refractory Archaean peridotite cumulates: Petrology and geochemistry of the Seqi Ultramafic Complex, SW Greenland, *Geoscience Frontiers*, *9*(3), 689-714. https://doi.org/10.1016/j.gsf.2017.05.003

Tamura, A., and S. Arai (2006), Harzburgite-dunite-orthopyroxenite suite as a record of supra-subduction zone setting for the Oman ophiolite mantle, *Lithos*, *90*(1-2), 43-56. https://doi.org/10.1016/j.lithos.2005.12.012

Tang, C., A. Webb, W. Moore, Y. Wang, T. Ma, and T. Chen (2020), Breaking Earth's shell into a global plate network, *Nature Communications*, *11*(1), 1-6. https://doi.org/10.1038/s41467-020-17480-2

Thakurta, J., E. M. Ripley, and C. Li (2008), Geochemical constraints on the origin of sulfide mineralization in the Duke Island Complex, southeastern Alaska, *Geochemistry, Geophysics, Geosystems*, *9*(7). https://doi.org/10.1029/2008GC001982

Topuz, G., E. Hegner, S. M. Homam, L. Ackerman, J. A. Pfänder, and H. Karimi (2018), Geochemical and geochronological evidence for a Middle Permian oceanic plateau fragment in the Paleo-Tethyan suture zone of NE Iran, Contributions to Mineralogy and Petrology, 173(10), 81. https://doi.org/10.1007/s00410-018-1506-x

Van de Löcht, J., J. Hoffmann, C. Li, Z. Wang, H. Becker, M. T. Rosing, R. Kleinschrodt, and C. Münker (2018), Earth's oldest mantle peridotites show entire record of late accretion, *Geology*, *46*(3), 199-202. https://doi.org/10.1130/G39709.1

Van de Löcht, J., J. Hoffmann, M. Rosing, P. Sprung, and C. Münker (2020), Preservation of Eoarchean mantle processes in~ 3.8 Ga peridotite enclaves in the Itsaq Gneiss Complex, southern West Greenland, *Geochimica Et Cosmochimica Acta*, *280*, 1-25. https://doi.org/10.1016/j.gca.2020.03.043

Van Kranendonk, M. J. (2010), Two Types of Archean Continental Crust: Plume and Plate Tectonics on Early Earth, *American Journal of Science*, *310*(10), 1187-1209. https://doi.org/10.2475/10.2010.01

Van Kranendonk, M. J., W. J. Collins, A. Hickman, and M. J. Pawley (2004), Critical tests of vertical vs. horizontal tectonic models for the Archaean East Pilbara Granite-Greenstone Terrane, Pilbara Craton, Western Australia, *Precambrian Research*, *131*(3-4), 173-211. https://doi.org/10.1016/j.precamres.2003.12.015

Van Kranendonk, M. J., R. H. Smithies, A. H. Hickman, and D. C. Champion (2007), Review: secular tectonic evolution of Archean continental crust: interplay between horizontal and vertical processes in the formation of the Pilbara Craton, Australia, *Terra Nova*, *19*(1), 1-38. https://doi.org/10.1111/j.1365-3121.2006.00723.x

Völkening, J., T. Walczyk, and K. G. Heumann (1991), Osmium isotope ratio determinations by negative thermal ionization mass spectrometry, *International Journal of Mass Spectrometry and Ion Processes*, *105*(2), 147-159. https://doi.org/10.1016/0168-1176(91)80077-Z

Wager, L. R., and G. M. Brown (1967), *Layered igneous rocks*, WH Freeman.

Wal, D. V. d., and R. L. Vissers (1993), Uplift and emplacement of upper mantle rocks in the western Mediterranean, *Geology*, *21*(12), 1119-1122. https://doi.org/10.1130/0091-7613(1993)021<1119:UAEOUM>2.3.CO;2

Wang, Z., H. Becker, and T. Gawronski (2013), Partial re-equilibration of highly siderophile elements and the chalcogens in the mantle: A case study on the Baldissero and Balmuccia peridotite massifs (Ivrea Zone, Italian Alps), *Geochimica Et Cosmochimica Acta*, *108*, 21-44. https://doi.org/10.1016/j.gca.2013.01.021

Webb, A. A. G., T. Müller, J. Zuo, P. J. Haproff, and A. Ramírez-Salazar (2020), A non–plate tectonic model for the Eoarchean Isua supracrustal belt, *Lithosphere*, *12*(1), 166-179. https://doi.org/10.1130/L1130.1

Wheeler, J., D. Prior, Z. Jiang, R. Spiess, and P. Trimby (2001), The petrological significance of misorientations between grains, *Contributions to Mineralogy and Petrology,141*(1), 109-124. https://doi.org/10.1007/s004100000225

Wiemer, D., C. Schrank, D. Murphy, L. Wenham, and C. Allen (2018), Earth's oldest stable crust in the Pilbara Craton formed by cyclic gravitational overturns, *Nature Geoscience*, *11*(5), 357-361, doi:10.1038/s41561-018-0105-9. https://doi.org/10.1038/s41561-018-0105-9

Williams, I. R. (1999), Geology of the Muccan 1:100 000 sheet, Geological Survey of Western Australia.

Yao, Z., K. Qin, Q. Wang, and S. Xue (2019), Weak B-Type Olivine Fabric Induced by Fast Compaction of Crystal Mush in a Crustal Magma Reservoir, *Journal of Geophysical Research: Solid Earth*. https://doi.org/10.1029/2018JB016728

Yin, A. (2012a), An episodic slab-rollback model for the origin of the Tharsis rise on Mars: Implications for initiation of local plate subduction and final unification of a kinematically linked global plate-tectonic network on Earth, *Lithosphere*, *4*(6), 553-593. https://doi.org/10.1130/L195.1

Yin, A. (2012b), Structural analysis of the Valles Marineris fault zone: Possible evidence for large-scale strike-slip faulting on Mars, *Lithosphere*, *4*(4), 286-330. https://doi.org/10.1130/L192.1

Zuo, J., A. A. G. Webb, S. Piazolo, Q. Wang, T. Müller, A. Ramírez-Salazar, and P. J. Haproff (2021), Tectonics of the Isua Supracrustal Belt 2: Microstructures Reveal Distributed Strain in the Absence of Major Fault Structures, *Tectonics*, *40*(3), e2020TC006514. https://doi.org/10.1029/2020tc006514